Energy Storage Materials 86 (2026) 105001

Contents lists available at ScienceDirect

Energy Storage Materials

journal homepage: www.elsevier.com/locate/ensm

Data-driven surrogate modelling and calibration of particle breakage in Li-ion electrode calendering

Jiashen Chen [a], Maryam Asachi [b], Ali Hassanpour [c], Meisam Babaie [a], Masoud Jabbari [a,*]

[a] School of Mechanical Engineering, University of Leeds, Leeds LS2 9JT, UK
[b] School of Civil Engineering, University of Leeds, Leeds LS2 9JT, UK
[c] School of Chemical and Process Engineering, University of Leeds, Leeds LS2 9JT, UK

ARTICLE INFO

Keywords:
Lithium-ion batteries
Electrode calendering
Particle breakage
Dem modelling
Machine learning

ABSTRACT

This study introduces a comprehensive, data-driven framework for efficient simulation and calibration of particle breakage during lithium-ion battery electrode calendering. We first proposed a Discrete Element Methode (DEM) based spherical damage model realised via a particular particle replacement mechanism, and generated a broad training set by uniformly varying eight model parameters. On this basis, a novel dual-branch neural network is trained to reproduce both the full compaction-pressure profile and the statistical distribution of fracture events, achieving high fidelity against held-out simulations. This surrogate model is embedded within a two-stage inverse-optimisation routine that infers breakage parameters directly from experimental pressure-depth data, yielding calibrated inputs for rapid forward prediction. With the help of surrogate efficiency, a global Sobol analysis quantifies the relative importance of each parameter, guiding model simplification work and highlighting the roles of characteristic size and fracturing fitting exponent. The coupled DEM-Multilayer Perceptron (MLP) studies reveal that allowing particle breakage during heavy calendering appreciably lowers tortuosity and enhances effective diffusivity compared to non-fracturing scenarios, with larger initial particle sizes further improving transport pathways. Collectively, this work delivers a scalable and advanced approach for parameter estimation, sensitivity assessment, and design optimisation of electrode microstructures under realistic processing conditions.

List of Abbreviations

AM	Active Material
CB	Carbon Black
CBD	Carbon Binder Domains
DEM	Discrete Element Method
EEPA	Edinburgh Elasto-Plastic Adhesive
KL	Kullback-Leibler Divergence
LIBs	Lithium-Ion Batteries
ML	Machine Learning
MLP	Multilayer Perceptron
MSE	Mean Square Error
NMC	Lithium Nickel Manganese Cobalt Oxide
PCA	Principal Component Analysis
PSDs	Particle Size Distributions

1. Introduction

Under the dual imperatives of sustainability and global climate improvement, energy storage technologies have become critical to both the automotive industry and broader economic growth. Over the past decades, Lithium-ion Batteries (LIBs) have emerged as one of the most widely deployed solution in the energy field. However, as their adoption has surged, performance demands have increased in parallel [1]. End users and industry stakeholders now expect higher energy density, faster charge-discharge rates, longer cycle life, and enhanced safety, all at reduced manufacturing cost [2]. Consequently, understanding how manufacturing parameters influence electrode structure and microscale electrochemical behaviour has become increasingly important [3,4]. Calendering represents a pivotal step in electrode fabrication, during which loose particles are compacted, driving substantial alterations in pore morphology and particle arrangement [5]. These microstructural changes directly affect ionic and electronic transport pathways and, in

* Corresponding author.
E-mail address: m.jabbari@leeds.ac.uk (M. Jabbari).

https://doi.org/10.1016/j.ensm.2026.105001
Received 30 September 2025; Received in revised form 17 February 2026; Accepted 20 February 2026
Available online 21 February 2026

turn, the overall performance of the battery [6,7].

Discrete Element Method (DEM) simulation has become a primary tool for modelling the mechanical behaviour of electrode particles and the evolution of their microstructure during calendering [8] and battery manufacturing in general [9]. The parameterisation strategy for calendering models introduced by Schreiner et al. [10] has since become widely adopted and charted a clear research path in this field. They innovatively examine in detail how each model parameter influences the load-displacement response during calendering. In their work, nano-indentation experiments were utilised to calibrate key mechanical parameters, such as compressive strength, elastic rebound, and initial interparticle cohesion. The study also highlighted the critical role of particle-particle contact parameters. Their parameterisation framework and calibration methodology represented a pioneering advance for DEM models, significantly broadening the scope and reliability of virtual electrode fabrication studies. Subsequently, Ge et al. [11,12] further investigated the use of DEM for this application by integrating real cathode microstructural data obtained via X-ray computed tomography into their simulation framework. Their model enables tracking changes in porosity and tortuosity throughout the calendering process and quantitatively evaluates the fabric tensor and stress tensors of the electrode material, thereby revealing spatial heterogeneity and anisotropy in structural deformation. By coupling the DEM framework with a binder-phase generation algorithm, they were also the first to predict the tortuosity of calendered electrodes, demonstrating the model's potential to guide the design of electrode architectures for improved battery performance. Building on these foundational studies, Nikpour et al. [13], Lundkvist et al. [14], and Lippke et al. [15] further examined how the shape of both Active-Material (AM) and Carbon-Binder (CB) particles influenced the mechanical behaviour of calendered electrodes. They found that, while calendering outcomes varied with particle morphology, the dominant factor governing the elastic and plastic response was particle radius. Nevertheless, particle anisotropy may still have important implications for the electrode's electrochemical performance [16].

While fractured particles are generally considered detrimental to battery performance, potentially compromising the structural integrity and cycling lifespan of LIB, recent studies suggest that under specific conditions, they might also offer some beneficial effects on electrochemical performance [17,18]. These seemingly contradictory observations highlight the complex and multifaceted role of particle fracture in electrode behaviour, necessitating more nuanced modelling approaches. However, a significant challenge in accurately modelling these phenomena using the DEM lies in its fundamental assumption: DEM typically treats particles as ideal rigid bodies during calculations. Although prior research has attempted to represent AM and CB using non-spherical particles, the accurate simulation of particle deformation and, more critically, fracture during the calendering process, particularly under the high-pressure conditions typical of electrode manufacturing, remains a prominent unresolved issue. Over recent years, a few of researchers have attempted to offer solutions to this problem, including Xu et al. [19,20] and Orefice et al. [21], who proposed that constructing AM particles from a large number of extremely small secondary particles, mimicking their true morphology, could effectively simulate the extrusion, deformation, and fracture processes of particles under high-pressure conditions. Nevertheless, it is undeniable that this approach necessitates the creation of a substantial quantity of secondary particles (approximately hundreds of secondary particles) to construct a single realistic AM particle at the initial stage of simulation. This not only demands immense computational resources but also presents considerable challenges for calibrating the entire simulation.

The Tavares UFRJ breakage model, developed by Tavares et al. [22], is a mature sphere-based particle replacement strategy model that accounts for the stochastic and size-dependent nature of particle fracture energy, damage accumulation in particles, and the conservation of volume, mass, and energy before and after breakage. Its operational principle involves replacing a parent particle with several spherical progeny particles at the time step when breakage is detected, mimicking the fragmentation process. This model offers significant computational advantages over full-bonded particle models, which require continuous resolution and interaction calculations for all secondary particles throughout the simulation. In contrast, the Tavares UFRJ model is projected to reduce the total number of particles created by two orders of magnitude, with only a slight reduction in simulation speed occurring after a large number of particles have fractured within the system. Despite these benefits, applying the Tavares UFRJ model to micron-scale electrode particles presents considerable challenges, given the limited amount of research available on this topic, most of which has focused on simulating larger materials, such as rocks. Furthermore, a significant challenge lies in the difficulty of conducting precise single-particle crushing experiments, which are essential for calibrating a large number of fitting parameters of the breakage model. For micron-scale electrode particles, such experiments are exceptionally complex due to the minuscule size of the particles and the need for highly controlled, isolated force application and deformation measurement [23]. This experimental hurdle directly impedes the accurate parameterisation and validation of the breakage model for battery electrode applications.

The rapid advancements in Machine Learning (ML) offer a promising avenue for overcoming the aforementioned challenges in DEM simulations of electrode calendering. Researchers such as Vijay et al. [24], Galvez-Aranda et al. [25], and Duquesnoy et al. [26] have already begun to integrate ML models into this domain. Extensive research demonstrates that training ML models on data generated from physical simulations can effectively achieve rapid multi-objective optimisation and inverse design of LIB manufacturing parameters [27]. This approach also provides crucial insights into the microstructural evolution during compaction, significantly enhancing both the efficiency and scalability of the simulations.

Building on these advances, the present study introduces a novel deep-learning framework that integrates multi-objective optimisation with inverse parameter inference to support and validate DEM-based electrode calendering models. Using simulation data generated with the Tavares UFRJ breakage model, our network is trained to predict both the global compaction pressure curve and the local particle breakage-size distribution simultaneously. A bespoke loss function balances the mean-squared pressure error, the Kullback-Leibler divergence of the distribution, boundary penalty, and centroid alignment terms, ensuring the accurate reproduction of both macroscopic and microscopic behaviours. After training, the network's inverse-optimisation module automatically infers the optimal breakage parameters for newly observed pressure and distribution data, providing a fast and reliable calibration tool. We demonstrate that this approach not only captures the stress-induced fracture and plastic deformation of AM particles during compression, but also preserves pore-network connectivity and transport properties more effectively than models that do not account for fracture. To our knowledge, this study is the first to investigate the application of the particle replacement-based breakage model within the DEM modelling framework for lithium-ion electrode calendering field, offering a powerful new methodology for precise model parameterisation and comprehensive simulation validation.

2. Methodology

The experimental data for the cathode material used in this study were obtained from Sample C1 reported by Zhang et al. [28]. The initial conditions for the model presented in this work are based on the test results reported by them. The initial thickness of the electrode was 75μm, with a density of 2.56 g/cm^3 and a porosity of 41.42 %. The composition of the electrode was 94 wt. % NMC622 ($LiNi_{0.6}Mn_{0.2}Co_{0.2}O_2$) and 6 wt. % carbon black. Electrode calendering was performed using a production-scale double-roll compactor, equipped with rollers of 900 mm in diameter and 1300 mm in width,

operating at a rolling speed of 5m/min.

2.1. DEM modelling

In the Discrete Element Method (DEM), the displacement and rotation of individual particles are described in these two equations:

$$m^k\frac{dv^k}{dt} = F_b^k + F_p^k \tag{1}$$

$$I^k\frac{d\omega^k}{dt} = M_b^k + M_p^k \tag{2}$$

where m denotes the mass of a single particle, and I denotes its rotational inertia. v and ω represent the displacement velocity and the angular velocity of the particle, respectively. F_b describes the bonding force of the CBD phase, and M_b describes its robust torque. F_p is the contact force between neighbouring particles, and M_p is the contact torque originating from particles in tangential contact as well as rolling friction. The superscript k represents the k^{th} particle in the structure.

This study uses Altair EDEM high-performance simulation software to build DEM models of electrode structures. The base parameters used for the model are shown in Table 1.

The model domain represents the area where the simulation is carried out. Its size affects the model confidence, the total number of particles, and the length of time required for the simulation, etc. In this study, the size of the model domain was set to $100 \times 100 \times 200\mu$m after a comprehensive evaluation of computational costs and model accuracy. In this instance, the periodic boundary is defined in both X and Y directions, ensuring that particles will re-enter the model domain from the opposite side of the boundary once they have left it. Furthermore, particles in the vicinity of the boundary will interact with particles on the other side.

Above the model domain is a Z-direction movable steel plate to simulate the roller, and below the model domain is a stationary aluminium plate to simulate the current collector. The particle factory has the same dimensions as the model domain and operates in dynamic mode. The total mass is calculated based on the density of the coating, and AM and CB particles are generated at random locations at a speed of 5×10^{-3}kg/s and 1×10^{-4}kg/s, respectively. The diameter distribution of AM particles conforms to a normal distribution with a mean of 7.74μm and a standard deviation of 1.35μm ($X \sim N(7.74, 1.35^2)$), which is calculated based on the experimental data of Zhang et al. [28], whilst the diameter of CB particles is fixed at 3μm. Once the particles have been generated completely, they are initially stacked by gravity spontaneously. Following this, they are compacted by the pressure plate to the initial thickness of 75μm. Subsequently, the calendering simulation will be initiated (as shown in Fig. 1) with the time step of 4 % of the Rayleigh time step, in accordance with the requirement of the calculation accuracy and the limitation of the calculation conditions. The maximum amount of compression is set to 19.5μm. The coloured spheres denote AM particles whose diameters (4.94–10.69μm) are coded by the adjacent colour bar, and the grey spheres indicate CB particles. The transparent planes represent the calendering plates.

Table 1
DEM simulation input parameters.

Parameter	Unit	Value	Source
Particle density (AM), ρ_{AM}	kg/m ^{3}	4740	[28]
Young's modulus (AM), E_{AM}	GPa	168.30	[29]
Poisson ratio (AM), ν_{AM}	-	0.246	[29]
Particle density (CB), ρ_{CB}	kg/m ^{3}	2200	[30]
Young's modulus (CB), E_{CB}	GPa	0.65	[30]
Poisson ratio (CB), ν_{CB}	-	0.200	[30]
Coefficient of restitution, e	-	0.25	[28]
Particle static friction, $\mu_{p,s}$	-	0.12	[28]
Particle rolling friction, $\mu_{p,r}$	-	0.01	[28]
Plate Young's modulus (Steel), E_{St}	GPa	208	[11]
Plate density (Steel), ρ_{St}	kg/m ^{3}	7900	[11]
Plate Poisson's ratio (Steel), ν_{St}	-	0.3	[11]
Plate Young's modulus (Aluminium), E_{Al}	GPa	69	[11]
Plate density (Aluminium), ρ_{Al}	kg/m ^{3}	2700	[11]
Plate Poisson's ratio (Aluminium), ν_{Al}	-	0.3	[11]
Surface Energy (AM-AM)	J/m ^{2}	5	[10]
Surface Energy (AM-CB)	J/m ^{2}	20	[10]
Surface Energy (CB-CB)	J/m ^{2}	60	[10]

The Edinburgh Elasto-Plastic Adhesive (EEPA) model is widely used to characterise interactions between micron-sized particles. In this study, the EEPA model was used to capture the mechanical response of the electrode. The contact normal force $F_{n,p}$ between the particles equals the sum of the hysteresis spring force f_{hys} and the damping force f_{nd} times the unit normal vector n from the contact point to the centre of the particle:

$$F_{n,p} = \left(f_{\text{hys}} + f_{nd}\right)n \tag{3}$$

The force-displacement relationship of f_{hys} can be described in the following equation:

$$F_{\text{hys}} = \begin{cases} f_0 + k_1\delta^n & \text{if } k_2\left(\delta^n - \delta_p^n\right) \geq k_1\delta^n \\ f_0 + k_2\left(\delta^n - \delta_p^n\right) & \text{if } k_1\delta^n > k_2\left(\delta^n - \delta_p^n\right) > -k_{\text{adh}}\delta^n \\ f_0 - k_{\text{adh}}\delta^n & \text{if } -k_{\text{adh}}\delta^n \geq k_2\left(\delta^n - \delta_p^n\right) \end{cases} \tag{4}$$

where f_0 is the constant adhesion force, δ is the total normal overlap, δ_p^n is the plastic overlap, k_1 and k_2 are the loading and unloading stiffness, respectively, and k_{adh} is the adhesion stiffness. n is the non-linear index parameter, which is generally taken as 1.5 for electrode materials.

The loading stiffness k_1 can be expressed as:

$$k_1 = \begin{cases} 2E^*R^* & \text{if } n = 1 \\ \frac{4}{3}\sqrt{R^*E^*} & \text{if } n > 1 \end{cases} \tag{5}$$

where E^* and R^* represent the equivalent of Young's modulus and radius of particles i and j, respectively:

$$\frac{1}{E^*} = \frac{1-\nu_i^2}{E_i} + \frac{1-\nu_j^2}{E_j} \tag{6}$$

$$\frac{1}{R^*} = \frac{1}{r_i} + \frac{1}{r_j} \tag{7}$$

The contact plasticity ratio λ_p can be expressed as:

$$\lambda_p = \left(1 - \frac{k_1}{k_2}\right) \tag{8}$$

The impact of the contact plasticity ratio on the contact relationship between particles of different electrode materials in the EEPA model was in-depth examined by Schreiner et al. [10]. The optimal parameter settings reported in the literature have been used in this work (i.e., $\lambda_{p/\text{NMC\_NMC}} = 0.8$, $\lambda_{p/\text{NMC\_PVDF}} = 0.9$ and $\lambda_{p/\text{PVDF\_PVDF}} = 0.975$).

The damping force f_{nd} can be expressed as:

$$f_{nd} = -\beta_n v_n \tag{9}$$

β is the damping coefficient of the normal velocity. v_n is the relative normal velocity between particles. β_n can be calculated by the following equation, where e is the coefficient of restitution:

$$\beta_n = \sqrt{\frac{4m^*k_1}{1 + (\pi/\ln e)^2}} \tag{10}$$

m^* is the equivalent mass of particles i and j:

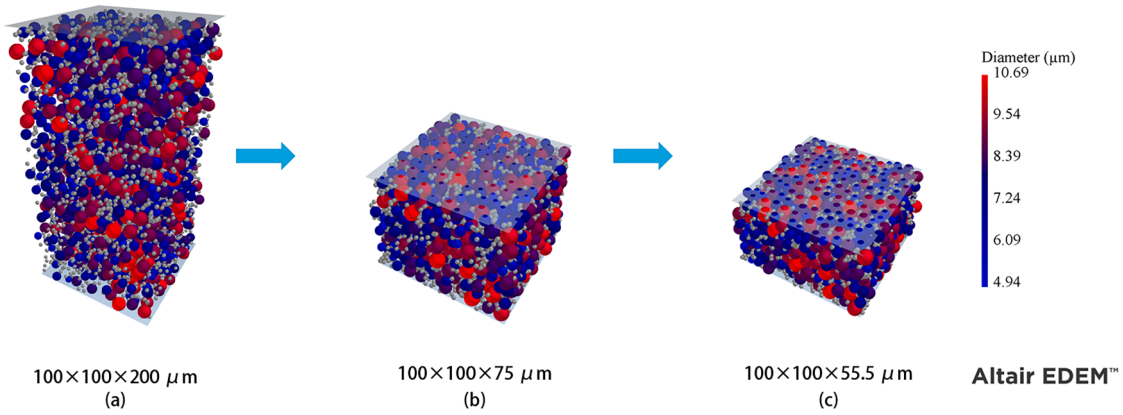

Fig. 1. Schematic of the DEM-based calendering process showing successive compression stages of the electrode microstructure: (a) initial uncompressed domain (100 × 100 × 200μm), (b) intermediate compression (100 × 100 × 75μm), and (c) final compression (100 × 100 × 55.5μm).

$$\frac{1}{m^*} = \frac{1}{m_i} + \frac{1}{m_j} \tag{11}$$

The contact tangential force $F_{t,p}$ between the particles is provided by the tangential spring force f_{ts} and tangential damping force f_{td}:

$$F_{t,p} = (f_{ts} + f_{td}) \tag{12}$$

The tangential spring force can be expressed as:

$$f_{ts} = (f_{ts(n-1)} + \triangle f_{ts}) \tag{13}$$

where $f_{ts(n-1)}$ is the tangential spring force at the previous time step, and the incremental tangential force $\triangle f_{ts}$ can be expressed as:

$$\triangle f_{ts} = -k_t v_t \triangle t \tag{14}$$

where k_t is the tangential stiffness of the particle, v_t is the tangential component of the velocity, and $\triangle t$ is the time step. The tangential stiffness k_t can be expressed as:

$$k_t = \xi_{t,m} \begin{cases} k_1 & \text{if } n = 1 \\ 8G^* \sqrt{R^* \delta_n} & \text{if } n > 1 \end{cases} \tag{15}$$

where $\xi_{t,m}$ is the tangential stiffness multiplier, and G^* is the equivalent shear modulus. For non-linear elastic contact springs, the recommended value of $\xi_{t,m}$ is 2/3 [31].

Similar to the calculation of the normal damping force f_{nd}, the tangential damping force f_{td} and tangential damping coefficient β_t can be calculated by the following equation:

$$f_{td} = -\beta_t v_t \tag{16}$$

$$\beta_t = \sqrt{\frac{4m^* k_t}{1 + (\pi / \ln e)^2}} \tag{17}$$

For the EEPA model, to describe the sliding friction, the critical tangential force f_{ct} is limited by the Cullen friction criterion, where μ is the coefficient of sliding friction:

$$f_{ct} \le \mu \left| f_{\text{hys}} + k_{\text{adh}} \delta^n - f_0 \right| \tag{18}$$

To describe the rolling friction, a torque needs to be applied to the contact surface of the particle, and the total torque η_i can be expressed as:

$$\eta_i = -\mu_r \left| f_{\text{hys}} \right| s_i \omega_i \tag{19}$$

where η_i is the coefficient of rolling friction, s_i is the distance from the contact point to the centre of the particle, and ω_i is the angular velocity at the contact point.

In this study, the behaviour of the binder was calculated using the bonding model developed by Potyondy and Cundall, which was originally used to describe the mechanical correspondence of the bonded phase between particles [32].

The normal force $F_{n,b}$ can be expressed as:

$$F_{n,b} = \left(F_{n(n-1),b} + \triangle F_{n,b}\right) \tag{20}$$

where $F_{n(n-1),b}$ is the bonding force at the previous time step, and $\triangle F_{n,b}$ is the incremental normal force, which can be expressed as:

$$\triangle F_{n,b} = -k_{n,b} v_{n,b} \triangle t \tag{21}$$

where $k_{n,b}$ is the normal stiffness of the bond, and $v_{n,b}$ is the normal component of the velocity.

Similarly, the calculation expression for the tangential spring force $F_{t,b}$ is:

$$F_{t,b} = \left(F_{t(n-1),b} + \triangle F_{t,b}\right) \tag{22}$$

$$\triangle F_{t,b} = -k_{t,b} v_{t,b} \triangle t \tag{23}$$

where $F_{t(n-1),b}$ is the bonding tangential force at the previous time step, $\triangle F_{t,b}$ is the incremental tangential force, $k_{t,b}$ is the tangential stiffness of the bond, and $v_{n,b}$ is the tangential component of the velocity.

The normal bond moments $M_{n,b}$ can be calculated from the incremental values with the time step:

$$M_{n,b} = \left(M_{n(n-1),b} + \triangle M_{n,b}\right) \tag{24}$$

The incremental normal bond moments $\triangle M_{n,b}$ can be expressed as:

$$\triangle M_{n,b} = -k_{n,b} A_b \omega_{n,b} \triangle t J_b \tag{25}$$

where A_b is the bond cross-sectional area, J_b is the polar moment of inertia of the bond, and $\omega_{n,b}$ is the relative angular velocity of the normal component.

The calculation expression for tangential bond moments $M_{t,b}$ and incremental tangential bond moments $\triangle M_{t,b}$ is similar to normal bond moments $M_{n,b}$ and incremental normal bond moments $\triangle M_{n,b}$:

$$M_{t,b} = \left(M_{t(n-1),b} + \triangle M_{t,b}\right) \tag{26}$$

$$\triangle M_{t,b} = -k_{t,b} A_b \omega_{t,b} \triangle t I_b \tag{27}$$

where I_b is the moment of inertia of the bond, and $\omega_{t,b}$ is the relative angular velocity of the tangential component.

The bond strength is defined by the beam theory and has a maximum

value:

$$\sigma_{n,b} = \frac{|F_{n,b}|}{A_b} + \frac{|M_{t,b}|R_b}{I_b} \leq \sigma_{n,st} \tag{28}$$

$$\sigma_{t,b} = \frac{|F_{t,b}|}{A_b} + \frac{|M_{n,b}|R_b}{J_b} \leq \sigma_{t,st} \tag{29}$$

where $\sigma_{n,b}$ and $\sigma_{t,b}$ are bond normal and shear stresses, $\sigma_{n,st}$ and $\sigma_{t,st}$ are bond normal and shear strength, respectively.

In this study, such virtual bonds are intentionally applied only around CB particles to provide a representative inter-particle cohesive force during the initial compression stage, when particle contacts are sparse, and the contact network is not yet fully developed. This treatment allows the early-stage stiffness to be captured while minimising artificial contributions to flow resistance that could arise from continuously regenerating bonds. As compression proceeds and the contact network becomes increasingly dense, binder rearrangement and reattachment effects are predominantly governed by surface energy-based contact parameters. The generation of bonds requires setting the contact radius for the particles. A bond is considered to have been generated when the centre-to-centre distance between two adjacent particles satisfies the following conditions.

$$\| P_A - P_B \| \leq \xi_b (R_A + R_B) \tag{30}$$

To ensure realistic inter-particle bonding in the initial phase, the bonding radius coefficient ξ_b is set to 1.5 in this study. This value, determined through iterative calibration against experimental results, balances the formation of sufficient adhesive bonds without inducing excessive connectivity, thereby reflecting the actual behaviour of binders in electrode structures.

2.2. Particle breakage method

This study applies the Tavares UFRJ breakage model [22] to describe the fracture behaviour of AM particles under high-stress conditions. The model comprises semi-empirical and semi-theoretical mathematical expressions that define the critical conditions for particle failure. Once a particle is determined to have fractured, it is instantly replaced by a cluster of smaller spherical particles. Each particle designated as breakable is assigned a specific fracture energy value, representing the maximum stress energy it can withstand before breaking. This fracture energy E conforms to the upper truncated lognormal distribution:

$$P_o(E) = \frac{1}{2}\left[1 + \mathrm{erf}\left(\frac{\ln E^* - \ln E_{50}}{\sqrt{2\sigma^2}}\right)\right] \tag{31}$$

where E_{50} and σ are the median and standard deviation of the lognormal distribution, respectively.

$$E^* = \frac{E_{max}E}{E_{max} - E} \tag{32}$$

where E^* is the upper limit of the distribution.

This breakage model takes into account the effect of particle size on fracture energy; as particle size decreases, the energy per unit mass required to break brittle particles increases:

$$E_{50,i} = \frac{E_\infty}{1 + k_p/k_s}\left[1 + \left(\frac{d_o}{d_i}\right)^{\varphi}\right] \tag{33}$$

where E_∞, d_o and φ are the model fitting parameters, which need to be determined based on the experimental results, and d_i is the representative particle diameter of the particles. k_p and k_s are the Hertzian stiffness of the particle and the stiffness of the surface of the device used to measure the fracture properties, respectively. They are calculated from the following formula:

$$k_{p,s} = \frac{Y}{1 - \upsilon^2} \tag{34}$$

Where Y is the Young's modulus and υ is the Poisson's ratio of the particle.

When the impact energy of a single event is less than the set fracture energy of the particle, it will suffer internal damage rather than break. At this point, the particle will have a lower specific fracture energy than before. This damage is calculated based on continuous damage mechanics:

$$E'_f = E_f(1 - D) \tag{35}$$

where E'_f is the specific fracture energy after damage, E_f is the specific fracture energy before damage, and D is an estimate of the extent of damage:

$$D = \left[\frac{2\gamma}{(2\gamma - 5D + 5)} \cdot \frac{eE_k}{E_f}\right]^{\frac{2\gamma}{5}} \tag{36}$$

where γ is the damage accumulation factor, eE_k is the effective specific impact energy, and e is the energy ratio involved in the collision calculation, which is related to the stiffness of the particle:

$$e = \frac{1}{1 + k_p/k_s} \tag{37}$$

E_k is the energy acquired by a particle after being subjected to a collision, defined by normal E_n and shear energy E_t:

$$E_k = E_n + c_t E_t \tag{38}$$

When the specific impact energy of a particle is much higher than its specific fracture energy, the particle is replaced by its fragments (Fig. 2). The degree of particle fragmentation can be quantified using the parameter t_{10}, which indicates the proportion of fragments smaller than 1/10 of the initial particle size. It is defined by the particle specific impact energy and the median fracture energy:

$$t_{10} = A\left[1 - \exp\left(-b'\frac{eE_k}{E_{50}}\right)\right] \tag{39}$$

where A and b' are the model fitting parameters.

2.3. Deep learning modelling

To generate training and testing data, this study employed Latin Hypercube Sampling (LHS) to perform stratified sampling within finite bounds for eight adjustable fitting parameters of the breakage model. Each parameter range was evenly divided into multiple strata, with one sample drawn from each stratum to ensure uniform coverage across the parameter space. A total of 280 initial parameter sets were generated and subsequently used to run automated simulations via Altair EDEM batch scripts Table 2.

The correlation heatmap analysis revealed that the absolute values of the pairwise correlation coefficients remained below 0.3 ($|r| < 0.3$), indicating low interdependence among parameters and confirming the dataset's suitability for training Fig. 3.

The training dataset comprises two components. First, it includes the evolution of compaction pressure over the entire electrode structure, which serves as the output for the pressure-prediction branch. Second, it contains the distribution of single-particle peak breakage load versus particle diameter, which serves as the output for the distribution-prediction branch. The compaction pressure data were obtained from 196 sequential, time-ordered sampling points recorded at the upper platen in EDEM during the compression process. To suppress high-frequency oscillations caused by instantaneous pressure spikes from particle breakage while preserving physically meaningful fracture-

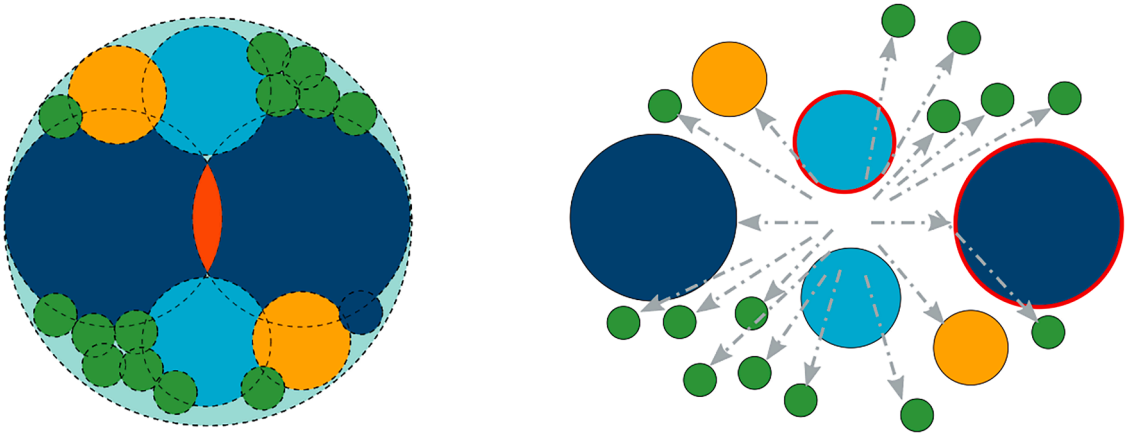

Fig. 2. Schematic illustration of particle replacement during the fracture process (Each colour represents a size) [33].

Table 2
DOE parameter design.

Parameter	Unit	Range
Damage constant,γ	-	1.0 - 10.0
E_{50} parameter,E_∞	J/kg	1500 - 3500
E_{50} parameter,d_0	μm	4.0 - 12.0
Fitting parameter,ϕ	-	0.10 - 3.50
Standard deviation,σ_E	-	0.10 - 1.00
Alpha percentage, A	%	20 - 85
Fracture parameter, b'	-	0.010 - 0.100
Truncation ratio, R_τ	%	80 - 100

driven peaks, these pressure traces were smoothed using a Savitzky-Golay filter:

$$y_i = \sum_{j=-m}^{m} c_j \, x_{i+j} \tag{40}$$

where the window length is $2m+1$, x_i is the original discrete signal, y_i is the smoothed signal, and c_j is the convolution coefficient. For a zero-order (smooth) Savitzky-Golay filter, the coefficient vector c is:

$$\begin{aligned} \mathbf{c} &= \mathbf{A}\left(\mathbf{A}^{\mathrm{T}}\mathbf{A}\right)^{-1}\mathbf{e}_0, \\ \mathbf{A} &\in \mathbb{R}^{(2m+1)\times(d+1)}, \\ \mathbf{A}_{k,p} &= k^p,\ k=-m,\ldots,m,\ p=0,\ldots,d. \end{aligned} \tag{41}$$

in which $\mathbf{A}$ is the Vandermonde matrix, $\mathbf{e}_0$ is the unit vector, and d is the degree of the polynomial to be fitted.

The distribution data were obtained by continuously tracking each particle's unique ID throughout the simulation. By monitoring each

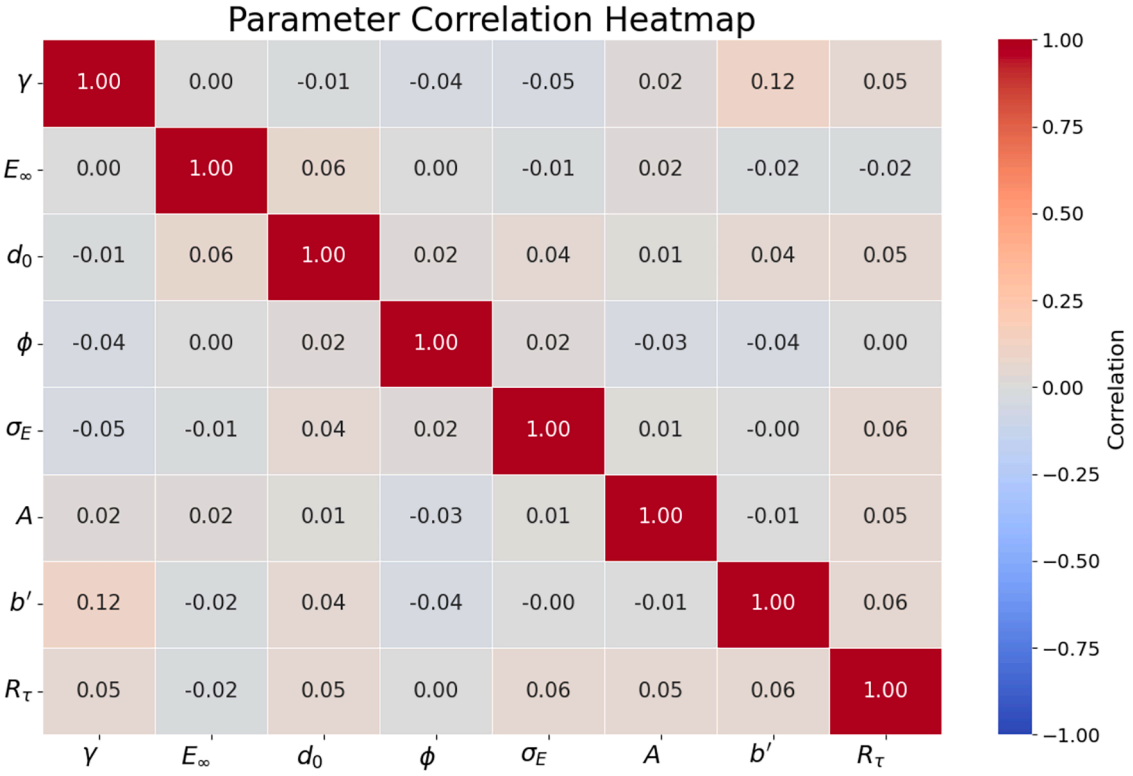

Fig. 3. Pearson correlation heatmap of eight input parameters generated by LHS. Each cell shows the pairwise Pearson correlation coefficient between two parameters used in the DEM simulations.

particle's presence at every time step, its final appearance marks the moment of fracture. For each fractured particle, the dataset records the peak load it sustained immediately before breakage, as well as its original diameter. This information complements the global pressure measurements by capturing the local mechanical limits and size dependence of individual-particle failure. Together, these two data streams provide complementary information for training the dual-branch predictive model.

Finally, the dataset was normalised to ensure consistency across simulations. Because the compaction pressure in a single run increases exponentially, a cube-root transformation was applied to the pressure data; this approach enhances resolution in the low-pressure regime while preserving fluctuations at higher pressures. Global minimum and maximum bounds were then used so that normalised pressures remain comparable across different simulation batches. As a result, each simulation produces a transformed pressure matrix:

$$S_{press} = (x_i)_{i=1}^{196} \tag{42}$$

where x_i is the filtered pressure value.

For the distribution data, a fixed 30 × 30 binning scheme was applied to discretise the particle breakage information. Within each bin, the number of broken particles was counted and converted into a proportion of the total, yielding a normalised distribution matrix:

$$S_{dist} = (a_{ij})_{i,j=1}^{30} \tag{43}$$

where a_{ij} is the probability density of particle breakage within each bin.

The exact global bin boundaries were enforced for all runs, guaranteeing that the resulting distribution matrices are directly comparable.

Multi-Layer Perceptron (MLP) is among the most widely adopted deep learning architectures, owing to its ability to learn complex nonlinear relationships, fast convergence on structured data, and relative ease of implementation and tuning [34]. These qualities make MLP particularly well suited for simultaneously predicting both the time-dependent compaction pressure and the particle peak-load distribution in electrode calendering. In this study, we therefore constructed a dual-prediction-branch MLP network composed of four main modules.

At the core of the shared feature extractor are two stacked residual blocks for feature refinement. Each block takes an input vector of dimension (in $_{dim}$) and produces an output of dimension (out $_{dim}$). Within the block, the main pathway applies a fully connected layer followed by a LeakyReLU activation (negative slope = 0.1) and dropout (rate = 0.3). In parallel, a skip connection projects the input directly (when the dimensions match) or applies a linear projection to align dimensions. The outputs of the main pathway and skip connection are summed and then normalised via layer normalisation. This residual design promotes robust gradient flow, allows the model to reuse lower-level features, and helps prevent degradation when stacking multiple layers. The shared feature extraction module begins by embedding the eight input parameters into a higher-dimensional space through a linear layer of size 256, followed by LeakyReLU activation and dropout. The output then passes through the two residual blocks described above, successively reducing the feature dimension from 256 to 128 to 64. These shared layers capture complex, non-linear interactions among the input parameters and produce a compact representation (size = 64) that serves as the foundation for both downstream tasks. From the shared 64-dimensional feature vector, the pressure prediction branch decodes the electrode's compaction profile in time. A linear layer expands the features to 128 neurons, followed by ReLU activation and dropout. A final linear layer then maps these units directly to the number of time steps (196). A Softplus activation on the output guarantees strictly positive pressure values while maintaining smooth gradients. The result is a continuous prediction of the compaction pressure sequence, shape (batch_size, 196), which directly corresponds to the DEM simulation experimental sampling points. At the same time, the particle-distribution prediction branch transforms the shared features into a two-dimensional histogram of peak load vs. diameter. First, features are projected to 256 neurons (with ReLU and dropout), then to 512 neurons (again with ReLU and dropout). To enforce a proper probability distribution over all bins, the matrix is flattened, passed through a Softmax across the 900 elements, and reshaped back to (30, 30). This yields a normalised distribution map that predicts the proportion of particles falling into each diameter-load bin for each sample Fig. 4.

All input data is encapsulated in a PyTorch dataset class. The constructor accepts three arrays: the eight-dimensional breakage parameters (parameter_vecs), the 196-point compaction pressure curves (pressure_vecs), and the 30 × 30 normalised distribution matrices (dist_matrices). Each array is converted to a torch.FloatTensor, for the distribution data, values are expanded by a small positive minimum (1×10^{-8}) to avoid numerical issues when taking logarithms. In the forward pass, the pressure prediction (pred_p) is compared to the true curve (true_p) via mean-squared error (MSE) Loss, emphasising average squared error. The predicted distribution (pred_d) is first logged (after expanding) and then measured against the true probability matrix (true_d) using Kullback-Leibler (KL) Divergence Loss. The final scalar loss is a weighted sum of these two components, and the module also returns each component separately for detailed monitoring. Losses are accumulated over each batch, and gradients are applied via the Adam optimiser. After processing all batches, average losses for both branches and the combined total are returned. To support real-time monitoring and post-hoc analysis, a lightweight collector gathers samples of true vs. predicted outputs during training and validation. For pressure curves, every batch is stored until a maximum of samples is reached. For distribution data, a random subset of each batch is sampled to avoid memory overflow. The collector can return concatenated arrays of true and predicted values, ready for visualisation.

The overall workflow is managed by an encapsulation function. It begins by instantiating the whole dataset and splitting it into training, validation, and test subsets in an 8:1:1 ratio. Data loaders are created with the chosen batch size. The model, loss function, and optimiser (Adam with weight decay) are assembled into a Trainer instance. Over a predefined number of epochs, the loop alternates training and validation, records detailed loss histories, and invokes the visualisation routine. After training concludes, final performance is evaluated on the held-out test set, and both the trained model and loss history are returned for downstream use.

Fig. 5 presents the iterative convergence of both MLP branches through PCA projection. After 80 epochs, the pressure-branch projections transition from a scattered distribution to a tight alignment along the line $y = x$, indicating increasingly accurate reconstruction of the true pressure curves. Simultaneously, in the distribution branch, the predicted data points progressively form an envelope that encompasses the original distribution points, demonstrating that the model's estimated probability maps not only capture the central tendency of the training data but also reflect its full variability. As training proceeds, the narrowing of the pressure-branch scatter implies reduced prediction error, while the emergence of the enveloping surface in the distribution-branch PCA plot confirms that the model successfully learns both the mean and spread of the underlying breakage distribution.

Table 3 summarises the loss performance for each branch. In the pressure branch, the MSE on the training set is slightly higher but still remains within a "low-error" range. The validation-set MSE is marginally lower, indicating that the model actually performs better on data that were not used for gradient updates. The test-set MSE is even lower, suggesting that the test data distribution is similar to, or perhaps easier to fit than, that of the validation set, possibly because the test data contain less noise or span a narrower range. Notably, there is no classic overfitting pattern of low training error and high validation/test error. Instead, the pressure branch appears to be nearly fully fitted and has achieved its primary optimisation goal.

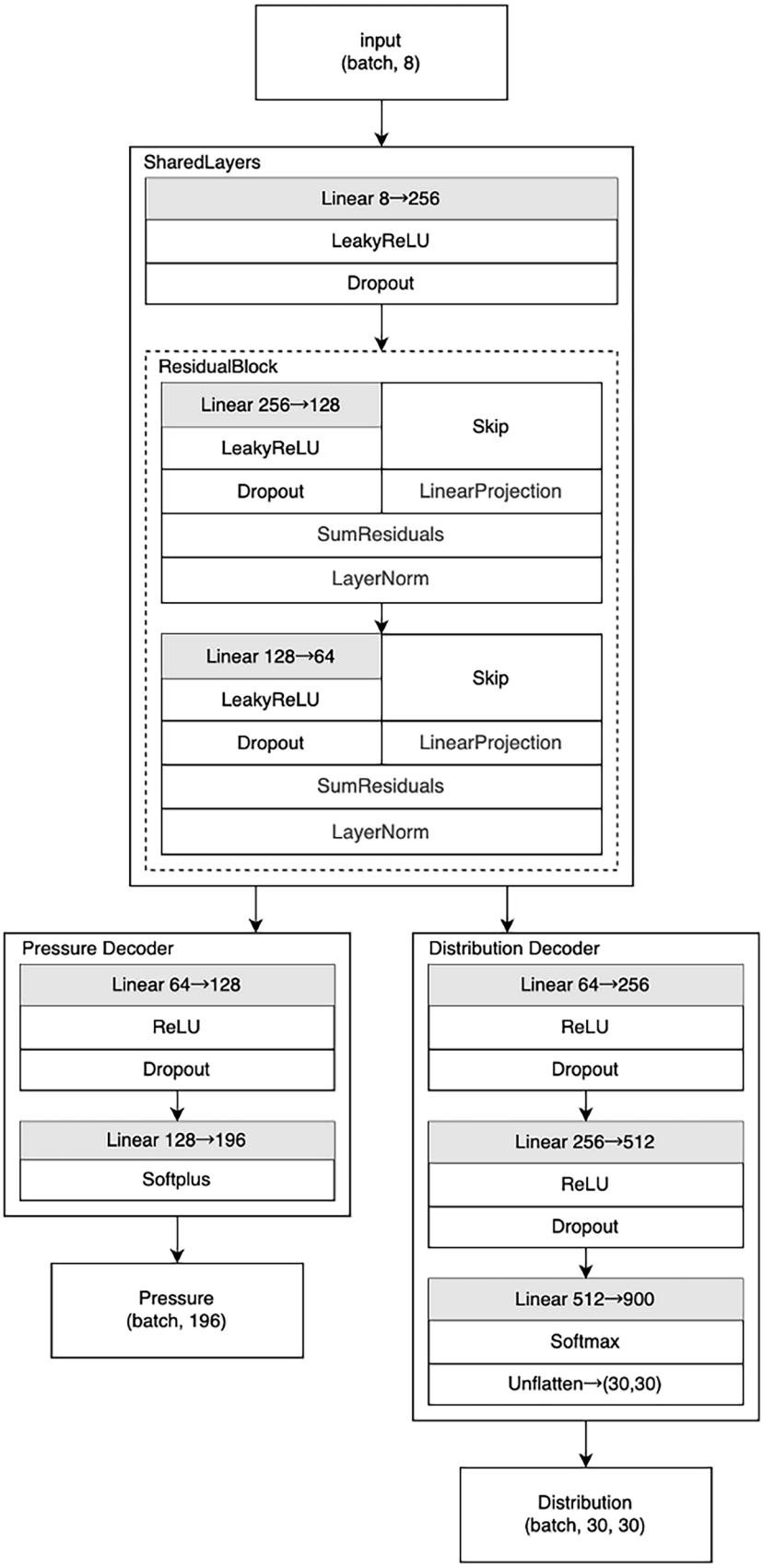

(caption on next page)

Fig. 4. Architecture of the dual-decoder multilayer perceptron used for predicting contact pressures and spatial force distributions. The network accepts an 8-dimensional input and first processes it through a shared feature extractor. Two sequential residual blocks then reduce the feature dimension, each comprising a fully-connected layer, LeakyReLU activation, dropout, a linear projection on the skip connection, residual summation, and layer normalisation. The resulting 64-dimensional embedding bifurcates into the Pressure decoder and the Distribution decoder. All linear layers are fully connected, and the dropout probability is set uniformly across the network.

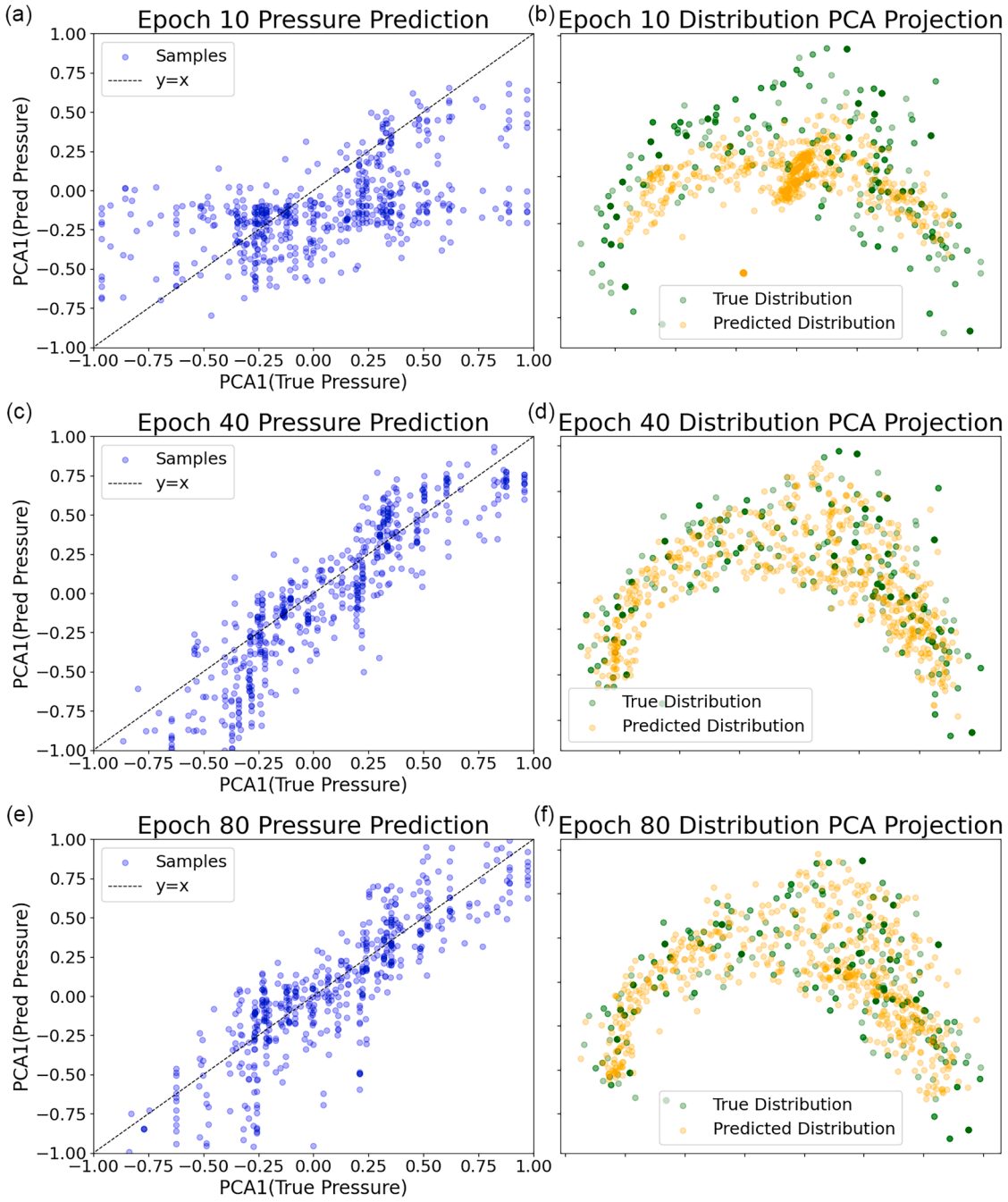

Fig. 5. PCA projections of the pressure and spatial-distribution predictions at different training epochs: (a, b) epoch 10; (c, d) epoch 40; and (e, f) epoch 80. Panels (a), (c), (e): Scatter plots of the first principal component (PC1) of true versus predicted calendering pressures. Each blue marker represents one sample; the black dashed line denotes the ideal $y = x$ correlation. Panels (b), (d), (f): Overlaid PCA projections of the true (green) and predicted (orange) spatial force distributions onto their first two principal components. Each semi-transparent point corresponds to the distribution of one sample.

For the distribution branch, the KL divergence errors follow the pattern: smallest on the training set, largest on the validation set, and intermediate on the test set. This trend indicates that the model fits the training distribution better than unseen data. However, because the test-set KL divergence is relatively close to the training-set value, this branch can also be regarded as approaching convergence. It is important to note, though, that due to the high noise level in the sample data and the inherently random nature of particle breakage, the distribution branch

Table 3
Overview of losses for each branch.

	Press. Branch	Dist. Branch	Weighted Total
Train Loss	0.0018	0.3000	0.0913
Val Loss	0.0011	0.3689	0.1114
Test Loss	0.0003	0.3300	0.0992

cannot reduce the overall KL divergence to a very low value during training. Consequently, this branch exhibits a certain degree of underfitting.

2.4. Reverse optimisation algorithm

Eight model parameters are initially maintained as a single nn. Parameter tensor with gradient tracking enabled. The initialisation strategy uses a Sobol quasi-random sequence to sample the [0, 1] hypercube evenly, providing a well-distributed starting point for optimisation. To keep parameter values strictly within [0, 1] throughout the process, a projection step clamps them after each update. This projection preserves gradient information while enforcing the required bounds. The hybrid optimisation strategy proceeds in two phases. First, an Adam optimiser explores the parameter space with a relatively large learning rate (0.05) for roughly 30 % of the total iterations, rapidly steering parameters toward regions of lower loss. Next, a limited-memory BFGS optimiser refines the solution with a smaller step size (0.01) over the remaining 70 % of iterations. In each phase, optimiser-specific "closure" functions compute the current predictions and loss, allowing limited-memory BFGS to perform its line-search updates and Adam to integrate gradient information.

During the reverse deduction process, the multi-term loss function aims to balance three objectives: a weighted Huber loss on valid pressure points (with an exponential weighting to emphasise higher loads), a distribution-centric penalty that biases the predicted matrix toward the specified centroids, and a boundary penalty that grows exponentially as any parameter approaches 0 or 1. Each term is scaled by adjustable weights that are automatically normalised to sum to unity. This composite loss drives the inversion to find parameter sets that simultaneously reproduce the target pressure profile, approximate the target distribution shape, and remain well within the valid range. To reduce sensitivity to initialisation, the entire two-phase optimisation is repeated for a specified number of random restarts. After each restart, the final loss is compared against the best loss seen so far. The algorithm retains the parameters corresponding to the lowest loss across all restarts. The final output is the best-found parameter vector, which can then be applied to forward simulations or further refined for improved accuracy.

3. Results and discussion

3.1. Binder behaviour analysis

In the initial stages of electrode calendering, the binder primarily serves to stabilise the local particulate structure, thereby restricting large-scale particle movement and flow during compression. However, as the calendering depth increases, the primary source of the reaction force exerted on the calendering rollers transitions from the resistance of the binder to flow to the elastoplastic deformation of the AM particles themselves. Consequently, the influence of the binder's cohesive forces becomes progressively negligible at higher compression ratios. The same mechanism is reflected in the behaviour of virtual bonds. As illustrated in Fig. 6(a), almost all particles in contact with CB particles are bonded in the initial state (the blue colour indicates that bonds are in effect). As the calendering process begins, the system gradually becomes more compact, and the inter-particle contacts begin to increase. However, because bonds are only established at the initial time step, newly formed contact interfaces between particles in subsequent calendering steps do not generate additional bonds, as indicated by the white segments in Fig. 6(b). As the compressive force increases, the forces acting upon the bonds also gradually increase. Once the force on a bond exceeds the predefined stiffness (3.5×10^{13}N/m^3) and strength (5×10^7Pa), the bond will break and cannot be regenerated afterwards. Broken bonds are represented by red segments in Fig. 6(c). With increasing calender intensity, the number of broken bonds increases correspondingly (Fig. 6 (d)), until the final stage of calendering (Fig. 6(e)). During compression, bonds absorb forces and exhibit plastic behaviour. However, at higher compression levels, the influence of bonds on the overall mechanical behaviour becomes progressively weaker.

The distribution of compressive forces experienced by AM particles during calendering reveals that, under low compression conditions (Fig. 7a,b), the presence of bonds significantly enhances the compressive stress on AM particles. This effect is consistent with the actual function of the CBD phase, which maintains structural stability at low pressure, reduces particle rearrangement, and keeps particle positions relatively fixed. However, as the extent of calendering increases (Fig. 7c, d), particle contacts become progressively tighter, and the impact of bonds on the compressive stress gradually diminishes. Eventually, under high compression conditions, the contribution of bonds to particle forces becomes negligible.

3.2. MLP-DEM coupling analysis

After a total of 500 iterations with three random restarts, the inversion optimiser inferred the optimal breakage model parameters from the experimental data, as shown in Table 4.

Three independent simulation experiments (R1, R2, and R3) were performed to assess both the stochastic nature and the reproducibility of the breakage model. For each experiment, the initial breakage parameters were supplied by the inverse-optimisation routine of the trained MLP network; all other initial settings and boundary conditions were kept identical. To reduce high-frequency noise from instantaneous fracture events, the raw compaction-pressure data were smoothed using a Savitzky-Golay filter with a third-order polynomial, a window size of 17 points, and a peak-correction threshold of 0.8.

The pressure-calendering degree curves are presented in Fig. 8.

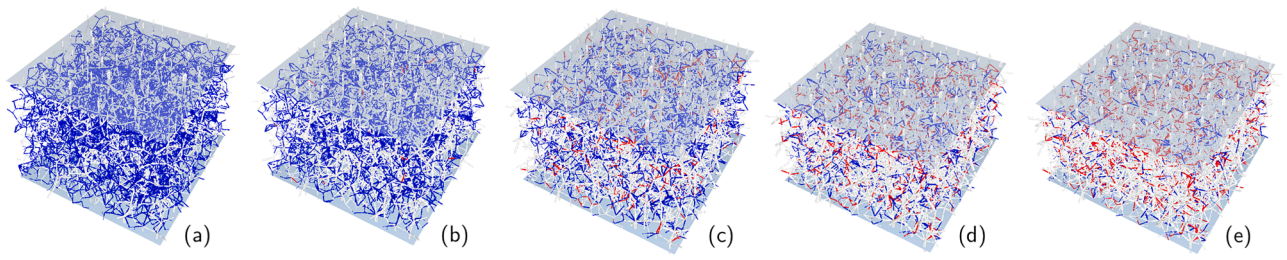

Fig. 6. Evolution of virtual-bond network during DEM calendering at increasing plate displacements: (a) 0μm (uncompressed), (b) 5μm, (c) 10μm, (d) 15μm, and (e) 19.5μm. Vector segments indicate the bonding status between contacting particles: intact virtual bonds are shown in blue; contacts that never formed a bond are shown in white; and broken virtual bonds are shown in red.

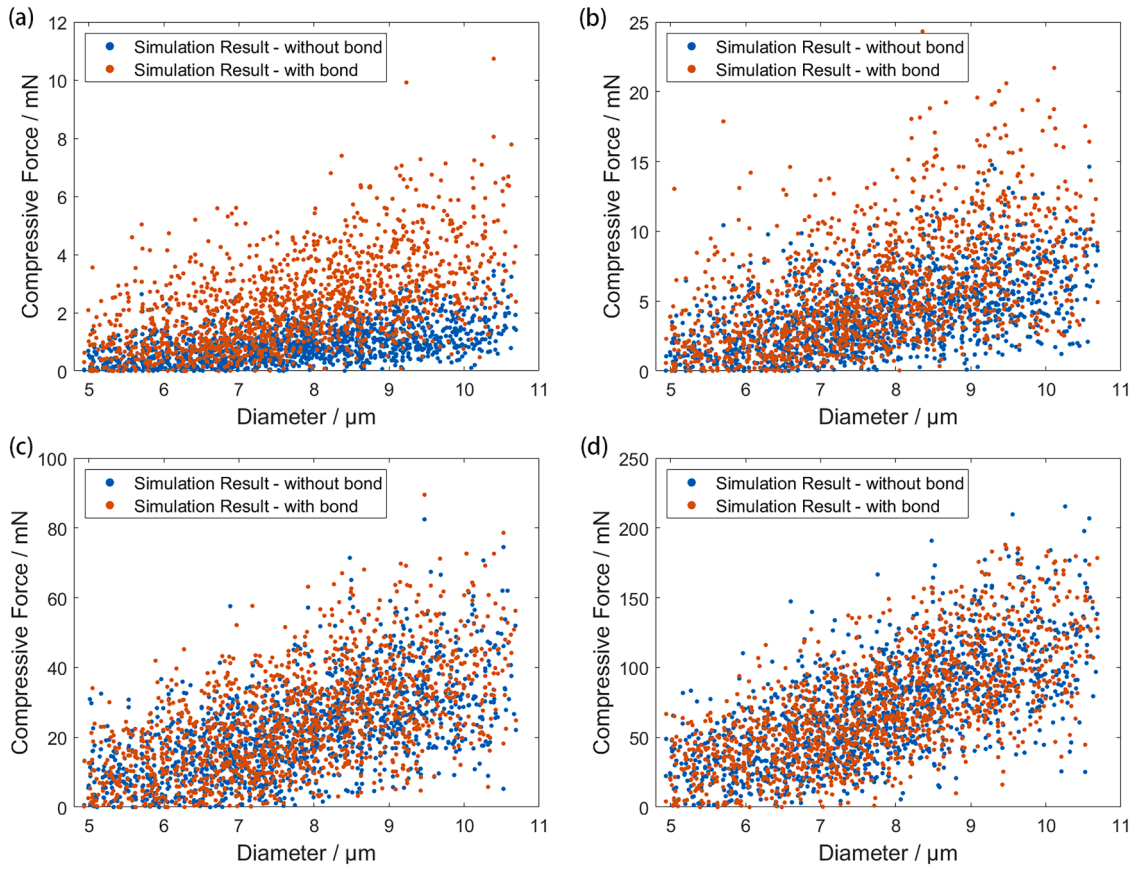

Fig. 7. Scatter plots of particle-scale compressive force versus AM particle diameter at successive calendering displacements: (a) 5μm, (b) 10μm, (c) 15μm, and (d) 19.5μm. Each data point represents the total surface normal force measured at an individual particle as a function of particle diameter.

Table 4
The optimal breakage model parameters from the MLP deep learning network inference.

Parameter	Unit	Value
Damage constant, γ	-	5.549
E_{50} parameter, E_∞	J/kg	2161
E_{50} parameter, d_0	μm	9.396
Fitting parameter, ϕ	-	2.587
Standard deviation, σ_E	-	0.947
Alpha percentage, A	%	34.274
Fracture parameter, b'	-	0.030
Truncation ratio, R_τ	%	89.928

Although each run exhibits some fluctuations in the high-pressure regime, attributable to the random timing and magnitude of individual particle fractures, the three curves largely coincide across the entire loading sequence (Fig. 8(a)). This high degree of overlap indicates that, despite microscale variability, the overall pressure response remains consistent. Furthermore, the MLP-predicted pressure profile closely traces the DEM-simulated results for all runs, demonstrating that the network reliably captures the global mechanical behaviour of the electrode during calendering (Fig. 8(b)).

The simulation of the loading curves demonstrates a satisfactory degree of agreement with the experimental results. These curves distinctly reveal the fracture points of particles (approx.80 MPa), marked by a transition in the pressure curve from exponential to linear growth. This transition indicates the onset of significant particle breakage, where the structural rearrangement of fractured particles begins to dominate the mechanical response of the system. Further compression leads to densification and increased contact between the particles, and when the pressure exceeds 250 MPa, additional particle rupture occurs. This study demonstrates that the DEM model effectively predicts the adverse effects of calendering on electrode structure under high-pressure conditions, including particle deformation and even fracture. These results highlight the capability of the model to capture critical mechanical behaviours, such as stress redistribution, force chain evolution, and particle failure mechanisms. The small residual discrepancies at the peaks do not compromise the overall fit, confirming that the MLP can generalise across different random realisations of fracture events.

Fig. 9(a)-(c) presents the normalised stress-diameter distribution matrices for R1, R2, and R3. While there are visible differences among the three matrices, reflecting the inherent randomness of particle breakage at the microscale, the centroids of each distribution overlap closely. Quantitatively, the centroid coordinates differ by <6.32 % in the stress dimension and 1.93 % in the diameter dimension across all three runs. In addition, the centroids predicted by the MLP network (Fig. 9(d)) for each experiment align closely with those computed from the DEM data. This agreement indicates that, although individual fracture events vary from run to run, the statistical centre of the breakage landscape remains stable and reproducible. The network's ability to predict these centroids further validates its effectiveness in capturing the average fracture behaviour.

Together, the three independent experiments demonstrate that, at the microscale, particle breakage exhibits a notable degree of randomness. However, when viewed at the macroscale, the compaction-pressure response and distribution-centroid location remain highly repeatable. This consistency confirms that the breakage model, when initialised with parameters derived from the MLP inverter, can reliably reproduce the electrode's mechanical response under calendering conditions. Consequently, the combined DEM-MLP framework offers a realistic description of a stable prediction of overall electrode behaviour,

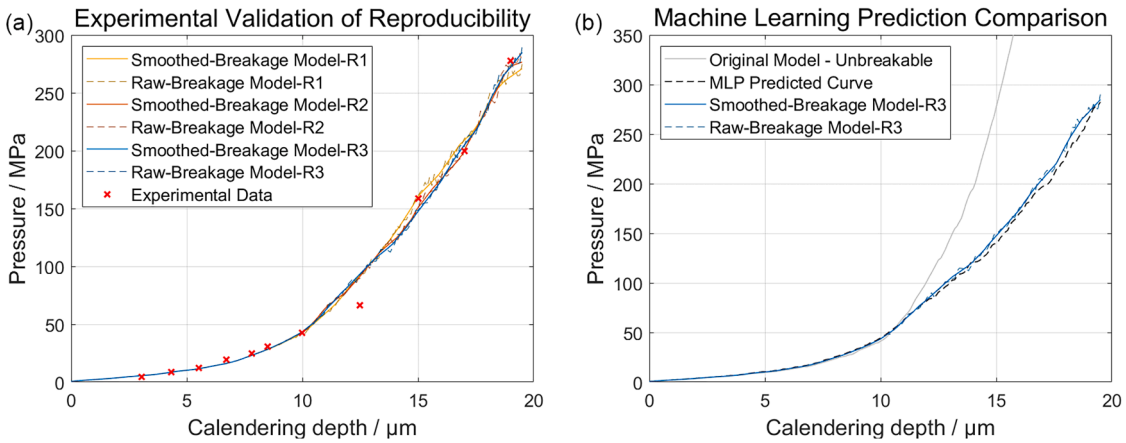

Fig. 8. Pressure-depth curves during electrode calendering comparing (a) the DEM breakage models, (b) the MLP surrogate, and the original (no-breakage) model. All experimental data are derived from Zhang et al. [28]. Continuous lines denote the smoothed pressure-breakage implementation; in contrast, dashed lines show the raw, unfiltered breakage response for each group.

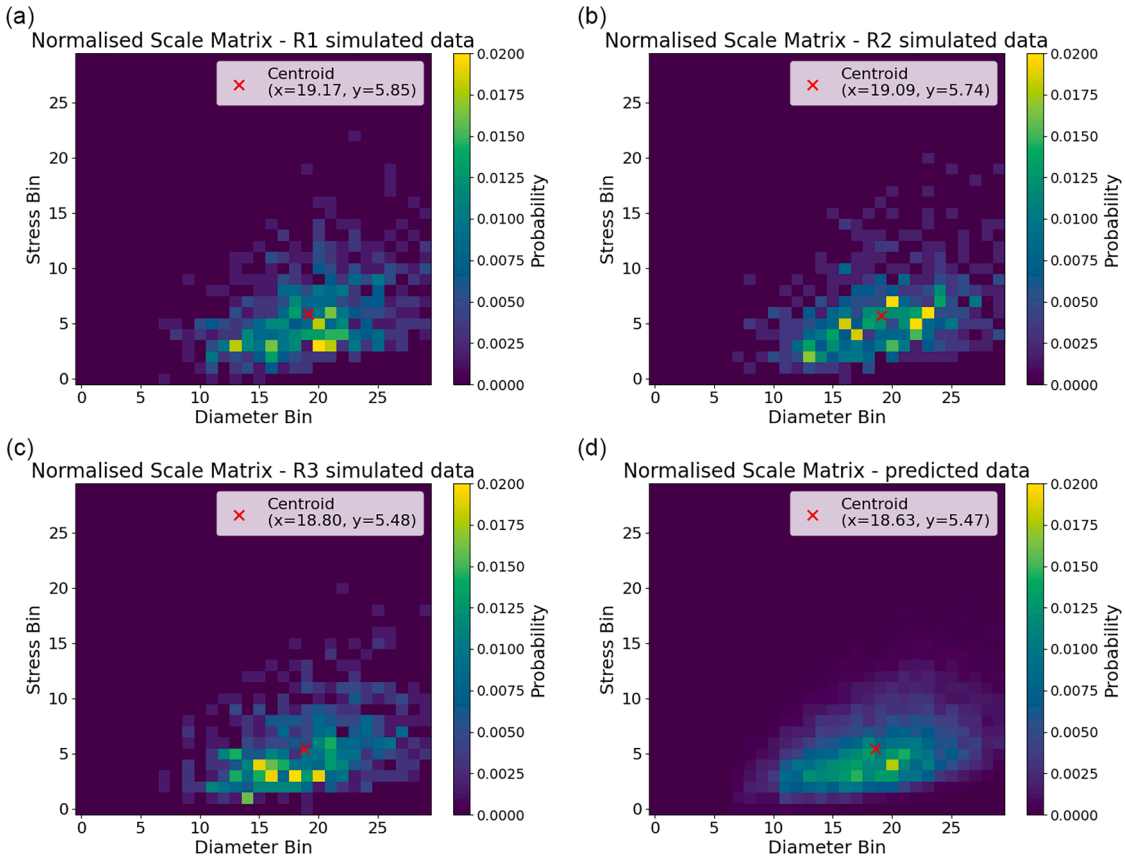

Fig. 9. Normalised scale matrices of particle breakage events in diameter-stress space for three DEM experiments and the MLP prediction. Panels show the probability of a breakage event occurring within each diameter bin (x-axis) and stress bin (y-axis): (a) Exp.R1, (b) Exp.R2, (c) Exp.R3, and (d) MLP-predicted distribution.

fulfilling the primary modelling objectives.

3.3. Parameter sensitivity analysis

After verifying the stability of the breakage model and the effectiveness of the deep learning model, the acceleration of the MLP model was employed to facilitate Sobol sensitivity analysis, which quantified the influence of each model parameter on four key output metrics. First, the peak pressure, which represents the maximum compaction load attained during calendering, reflects how strongly each parameter influences the overall process intensity. Second, the stress centroid, defined as the weighted mean of the breakage-distribution matrix along the stress axis, indicates the average stress level at which particles fracture (a lower value corresponding to a lower overall stress). Third, the diameter centroid, or the weighted mean along the particle-size axis, measures the tendency for larger particles to break (a higher value indicates a greater proportion of large-particle failure). Finally, the low-stress ratio, defined as the cumulative probability mass in the lowest one-third stress bins, quantifies the fraction of breakage events occurring under low stress. Fig. 10 presents the first-order and total-order

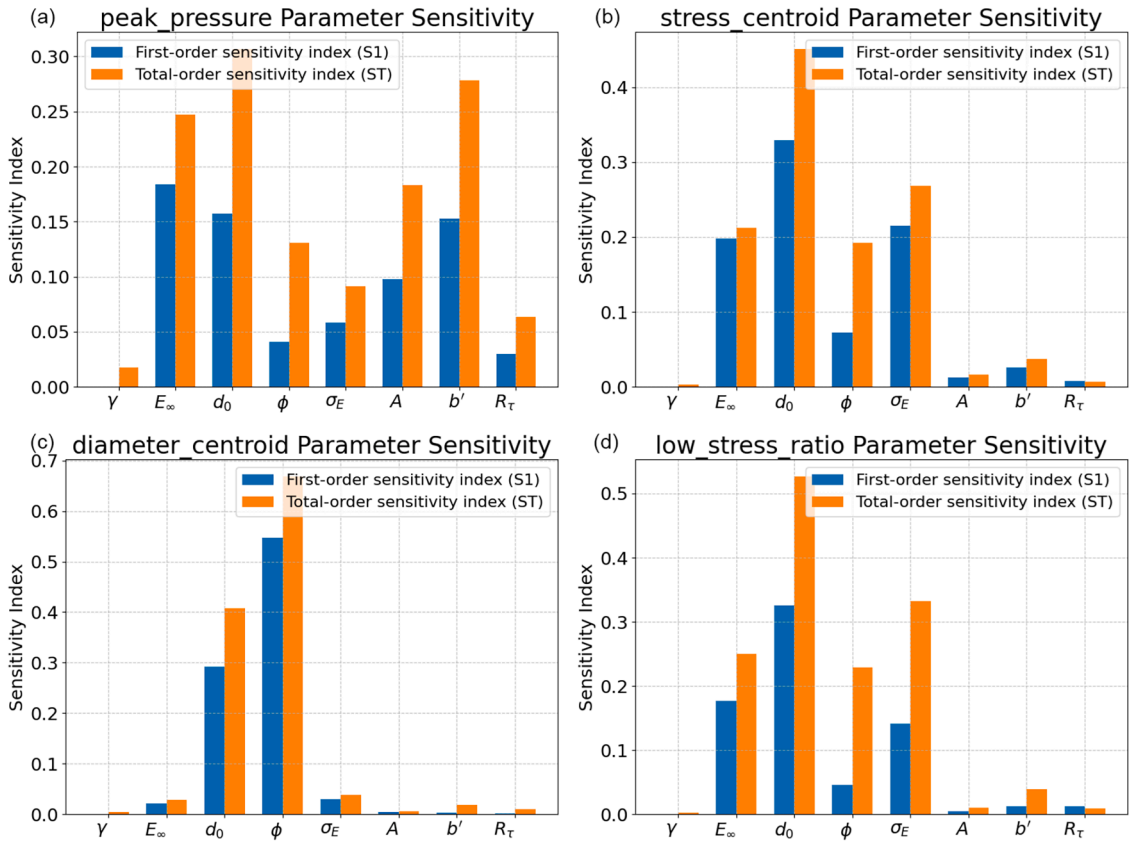

Fig. 10. Sobol sensitivity analysis of breakage model parameters for four key DEM outputs: (a) peak calendering pressure, (b) stress-centroid location, (c) diameter-centroid location, and (d) low-stress ratio. The first-order index (S_1) measures each parameter's direct effect on the output, while the total-order index (S_T) captures both direct and interaction effects.

Sobol indices for these four outputs, peak pressure (Fig. 10(a)), stress centroid (Fig. 10(b)), diameter centroid (Fig. 10(c)), and low stress ratio (Fig. 10(d)), revealing which parameters most strongly govern each aspect of the calendering response.

The Sobol analysis highlights d_0 as the single most influential parameter across all four outputs. Its first-order sensitivity (S_1) is consistently among the highest, and the gap between its total-order index (S_T) and S_1 is especially large. This indicates that d_0 not only exerts a strong main effect but also interacts significantly with other parameters, most notably ϕ and σ_E, so that simultaneous variation in d_0 and these parameters amplify output uncertainty. The factor ϕ dominates the variance in the diameter centroid: its S_1 exceeds 0.54 and its S_T reaches approximately 0.66, demonstrating both a large direct effect and nontrivial higher-order interactions. ϕ also exerts secondary influence on the stress centroid and the low-stress ratio, primarily through interactions with d_0 and E_∞. E_∞ and σ_E form a second tier of importance for the stress centroid and the low-stress ratio, each with first-order contributions in the range of 0.10–0.14 and total-order indices above 0.20. They also exert a moderate effect on peak pressure but have only a weak influence on the diameter centroid. Their substantial S_T-S_1 gaps reveal that they participate in nontrivial higher-order interactions, particularly with each other.

When examining each output specifically, peak pressure is governed principally by three parameters: b', d_0, and E_∞. Here, d_0 and b' share nearly equal first-order effects, with E_∞ slightly behind. Other parameters such as ϕ, σ_E, and A contribute only through interaction terms, while the Truncation ratio makes a minor direct contribution. For the stress centroid, d_0 almost single-handedly drives the variance; the next most important factors are σ_E, E_∞, and ϕ, but their first-order effects remain considerably smaller. Parameters b', A, Truncation ratio, and γ each register negligible sensitivity, either alone or in combination. In the case of the diameter centroid, ϕ is the clear leader, followed by d_0, with all other parameters, whether considered individually or through interactions, collectively accounting for <5 % of variance. This finding suggests that the physics governing large-particle breakage is effectively captured by just these two parameters. Finally, the low-stress ratio is again centred on d_0, whose S_1 is about 0.25 and S_T about 0.50, underlining its central role and strong interaction with other parameters. The next most influential parameters are σ_E, E_∞, and ϕ, each with first-order sensitivities around 0.10–0.14 and total-order indices exceeding 0.20. All remaining parameters contribute minimally.

Fig. 11 illustrates how the four key output indicators evolve as the eight breakage model parameters vary from 0 to 1. Based on the information provided by the trend chart and combined with the conclusions of the previous sensitivity analysis, it can be seen that: The parameter d_0 (Fig. 11(c)) exerts the strongest and most consistent influence on all four key outputs. As d_0 increases from 0 to 1, peak pressure and stress centroid both rise sharply, the low-stress ratio drops by >10 %, and the diameter centroid grows noticeably. Physically, a low d_0 value implies that particles break under lower stress, yielding a weaker overall structure, whereas raising d_0 shifts breakage to higher stresses, elevating both peak pressure and average fracture stress, and favouring the survival of larger fragments at low stress. The large gap between its total-order and first-order Sobol indices confirms that d_0 interacts strongly with other parameters (especially ϕ (Fig. 11(d)) and σ_E (Fig. 11(e))), amplifying output variance when they vary together.

Both E_∞ (Fig. 11(b)) and σ_E lie in the second tier of importance for stress-related metrics and the low-stress ratio. An increase in E_∞ raises peak pressure by roughly 0.13 and stress centroid by 0.07, while lowering the low-stress ratio by about 0.05; its effect on diameter

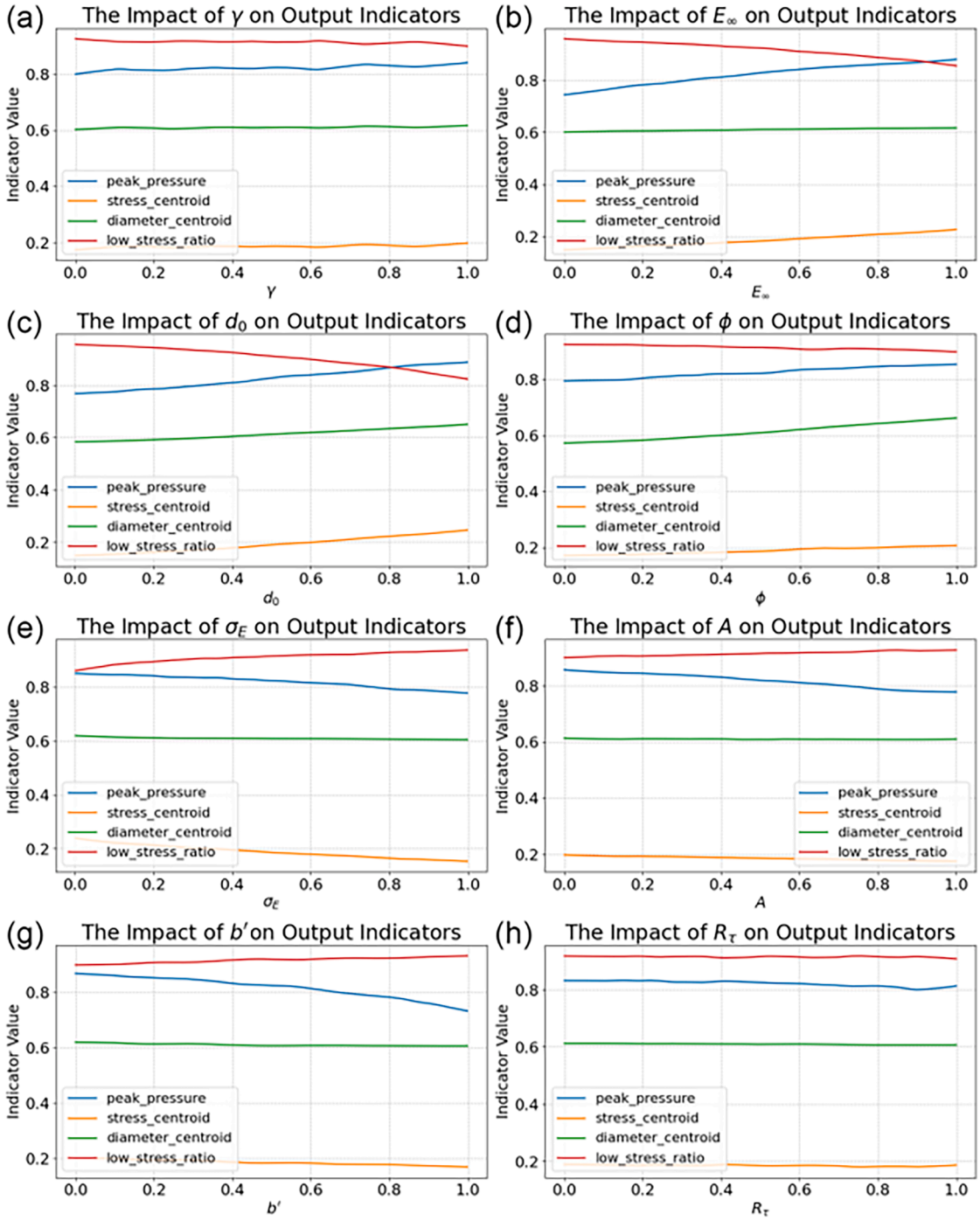

Fig. 11. Influence of individual breakage model parameters on four key output indicators. Each row of subplots shows the response of the outputs, peak calendering pressure (blue), stress-centroid location (orange), diameter-centroid location (green), and low-stress ratio (red), to a normalised variation (0 to 1) of one input parameter: (a) γ, (b) E_∞, (c) d_0, (d) ϕ, (e) σ_E, (f) A, (g) b', (h) R_τ. Across all subplots, the x-axis represents the parameter value, scaled linearly from its minimum to maximum sampling bounds, while the y-axis displays the resulting value of each output indicator. Steeper curves indicate stronger sensitivity to that parameter, while flat trends denote negligible influence.

centroid is minor (+0.02). A higher E_∞ means the system can store more elastic energy before failure, which both increases the fracture load and concentrates breakage at higher stress levels. Conversely, widening the breakage-threshold distribution (σ_E) reduces both peak pressure and stress centroid, slightly lowers the diameter centroid, and increases the low-stress ratio, since a broader distribution allows some particles to fail at lower stress. Other parameters, for example, A (Fig. 11(f)), b' (Fig. 11(g)), γ (Fig. 11(a)), and Truncation ratio R_τ (Fig. 11(h)), play relatively minor roles, which is consistent with the conclusions presented earlier. Increasing A gently reduces peak pressure (−0.07) and slightly raises the low-stress ratio (+0.04) without substantially affecting the centroids, suggesting it can be used to fine-tune the onset of low-stress breakage. The parameter B has a more pronounced effect on peak pressure (−0.14) and a small negative effect on stress centroid (−0.025), with negligible impact on diameter centroid; this indicates B can be adjusted to lower compaction loads without altering fragment size.

In summary, the dominant role of d_0, together with its strong interactions, suggests that rigorous experimental calibration of d_0 is crit-

ical to accurate model predictions. Fine-tuning ϕ, E_∞, and σ_E can then tailor the fragment-size distribution and stress response to meet specific performance targets. Parameters with negligible sensitivity (γ and Truncation ratio) may be fixed or removed to simplify the model. In future work, these insights could guide adaptive design of electrode formulations and calendering schedules, focusing experimental effort on the few parameters that most strongly govern both fracture mechanics and macroscopic strength.

3.4. Model robustness analysis

To evaluate the robustness of the proposed breakage model under varying AM particle size distributions (PSDs), a series of simulation experiments, designated C1-C4 and R4-R5, were conducted. Compared to the baseline simulation R1, experiments C1-C4 were designed to maintain a constant mean value for the normal distribution of AM particle sizes (subject to a negligible margin of error) while varying the standard deviation from 1.08 to 1.59 (Table 5). In contrast, simulations R4 and R5 involved simultaneous adjustments to both the mean particle size ($\mu_{R4} = 9.95\mu m$, $\mu_{R5} = 11.85\mu m$) and the standard deviation ($\sigma_{R4} = 1.67\mu m$, $\sigma_{R5} = 2.06\mu m$) relative to R1. To ensure consistency across all test cases, the total mass, volume, and intrinsic density of the active material were kept constant. Furthermore, the dimensions of the CB particles remained uniform throughout all simulations.

Fig. 12 presents the comparison of the PSDs for C1-C4 (Fig. 12(a)) and R4-R5 (Fig. 12(c)) against the baseline R1, alongside their corresponding mechanical response curves during the calendering process (Fig. 12(b), Fig. 12(d)). The simulation results indicate that the breakage model exhibits excellent robustness when subjected to a range of PSD variations. Specifically, the pressure-compaction curves across multiple groups show a high degree of consistency in their evolutionary trends. Although R4 and R5 manifest more pronounced pressure fluctuations in the high-stress regime, a detailed analysis of this phenomenon is provided in the subsequent section.

3.5. Electrode structure analysis

In this study, the tortuosity and effective diffusivity of the structures were quantified by first generating tomographic slice images from DEM simulations, which were subsequently processed and binarised using MATLAB and Python-based workflows. These processed images were then analysed using the TauFactor plugin within the PyTorch framework [35]. TauFactor calculates tortuosity and effective diffusivity by simulating diffusion processes and identifying the shortest effective transport pathways, thereby quantitatively evaluating the complexity and connectivity of the pore structure. This workflow effectively avoids the complicated and time-consuming meshing procedures typically associated with FEM, significantly reducing computational costs. Its primary advantage lies in the flexibility and efficiency with which it can rapidly analyse the system's porosity. Furthermore, this approach holds promise for integration with deep learning networks in future research, potentially enabling comprehensive predictive capabilities.

The simulation results show that, across all experiments, porosity (Fig. 13(b)), tortuosity (Fig. 13(c)), and effective diffusivity (Fig. 13(d)) exhibit clear, monotonic trends as compression increases. When the calendering reduction grows from 0 to 19.5μm, porosity falls sharply from approximately 42 % to about 22 %; tortuosity rises markedly from roughly 1.5 to between 1.9 and 2.3; and effective diffusivity declines from around 0.27 to the 0.10–0.18 range. These behaviours align with established observations in lithium-ion battery electrode calendering: densification reduces pore volume, lengthens and tortuates transport paths, and thereby increases diffusion resistance [27].

Although all experiments begin at nearly the same porosity (~42 %, due to identical particle mass and total volume), their initial tortuosity and diffusivity differ slightly. For example, R5 (mean AM diameter 12μm) has an initial tortuosity of 1.5640, higher than R1's (7.84μm) 1.5336, and a correspondingly lower diffusivity (0.2644 vs. 0.2773). This suggests that larger initial particle sizes produce a microstructure with marginally higher tortuosity and lower diffusivity, likely because fewer larger particles create slightly more curved pore channels. Nevertheless, in the early compression regime (0–5μm reduction), all three cases overlap closely, indicating that initial particle breakage (in breakage-model runs) has not yet occurred in significant quantity and microstructural changes are dominated by particle rearrangement and pore collapse.

In the moderate compression range (5–10μm), the three experiments continue to follow nearly identical trajectories: when porosity decreases to about 33 %, tortuosity increases to approximately 1.75, and diffusivity falls to around 0.19, with differences of only a few percentage points between cases. This convergence demonstrates that, during the initial densification phase (porosity 42 % to 33 %), whether particles fracture or what their initial size is has little effect on the bulk microstructure; reorganisation and pore compaction govern the behaviour.

However, beyond roughly 10μm of reduction (high-compression stage, 15–19.5μm), the results begin to diverge. Although porosity continues to decline in all experiments, ending at nearly identical levels (21.82–21.94 %), the evolution of tortuosity and effective diffusivity splits. The breakage model simulations (R1-R5) exhibit a more gradual rise in tortuosity and a slower decline in diffusivity compared to the non-fracture control (R0: original model). This divergence indicates that, once compression reaches a critical level, particle fracture generates secondary fragments that reshape the pore network, partially offsetting the deterioration of connectivity. Consequently, fracture delays the rate at which tortuosity increases and diffusivity decreases under heavy calendering.

At the maximum compression of 19.5μm, the impact of the breakage model becomes especially pronounced. In the non-fracture control (R0), tortuosity climbs to 2.2846, whereas in the breakage model case (R1) it remains at 1.8976, about 20 % lower. Likewise, effective diffusivity in R0 falls to only 0.1033, while R1 maintains a value of 0.1590, representing roughly a 50 % improvement under otherwise identical porosity (21.94 %). These differences arise because particle fracture alters the evolution of the pore network. In R0, intact AM particles withstand ever-increasing compaction pressures by deforming and rearranging without splitting. Large particles obstruct and constrict pore channels, forcing diffusion paths to navigate around solid spheres; as pressure increases, these detours become longer and more tortuous, sharply raising tortuosity and reducing diffusivity. Furthermore, without fracture, the material must bear higher global forces to achieve the same displacement (Fig. 8). Under such high loads, particles can undergo irreversible deformation, collapsing nearby pores and further impeding transport.

By contrast, in Experiment R1, a portion of AM particles fractures once a critical stress threshold is reached, producing multiple smaller fragments. This fragmentation benefits microstructure and transport in two main ways. First, newly created cracks and inter-fragment voids open fresh pathways: instead of circumventing whole particles, electrolyte can permeate through the gaps between fragments, effectively shortening diffusion distances and reducing tortuosity. Li et al. [36] and Nagda et al. [37] have also demonstrated that electrolytes can infiltrate

Table 5
AM particle size distribution data for multiple sets of simulation experiments. Unit: micrometre.

Experiment No.	Mean Value	Standard Deviation	D10	D50	D90
Sim.R1	7.743	1.349	5.902	7.746	9.563
Sim.C1	7.774	1.081	6.317	7.787	9.220
Sim.C2	7.696	1.419	5.749	7.637	9.708
Sim.C3	7.752	1.506	5.653	7.758	9.845
Sim.C4	7.767	1.589	5.528	7.765	9.958
Sim.R4	9.920	1.670	7.645	9.951	12.105
Sim.R5	11.854	2.061	9.080	11.847	14.599

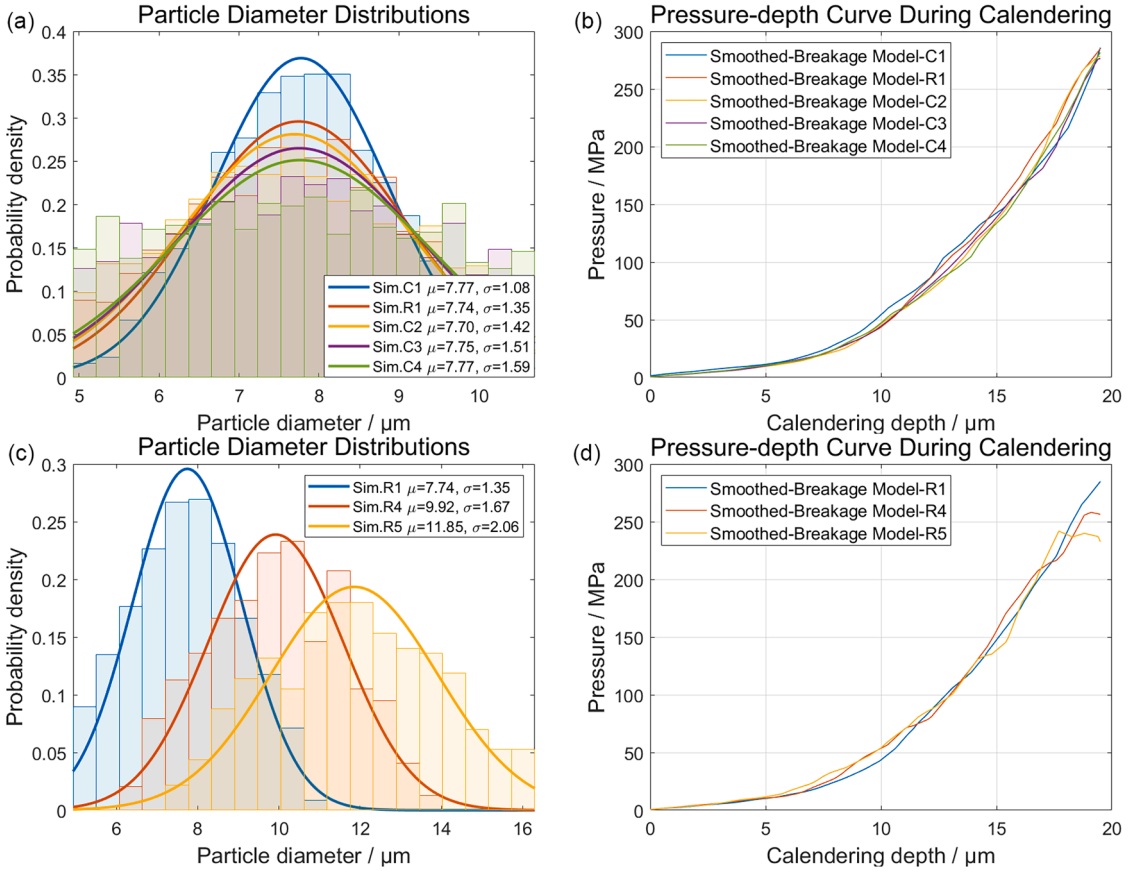

Fig. 12. Robustness analysis of the smoothed-breakage DEM model with respect to variations in the AM PSDs. Effect of difference in standard deviation of PSDs (a) on the calendering curve (b); effect of difference in mean value of PSDs (c) on the calendering curve (d).

newly formed cracks, thereby creating additional electrochemically active interfaces. This wetting effect alters the local ion-transport pathways, generating faster and more efficient channels for ionic conduction. Second, breaking large particles into smaller pieces lowers the macroscopic compaction resistance and facilitates more uniform particle rearrangement. Fragments can translate and rotate to fill the surrounding space more flexibly, avoiding the hard, point-contact packing of intact spheres that leads to extreme pore collapse. In fractured systems, a former pair of large particles may split into many smaller grains that interlock more evenly, preserving network connectivity without forming narrow, winding passages. Moreover, fracture relieves local stress concentrations [36]. In R0, contact forces concentrate at a few high-stress points, driving pore closure until irreversible deformation occurs. After particle breakage in R1, those stresses drop as fragments redistribute loads, so the overall compaction pressure required to reach 19.5μm is lower. Reduced loading prevents the extreme pore distortion seen in the non-fracture case and contributes further to the lower tortuosity in R1. Hence, particle breakage not only mitigates the rise in tortuosity under heavy calendering but also preserves effective diffusivity by creating new flow channels and reducing compaction resistance.

Larger initial particle sizes also alter the nature and extent of fracture during compression, leading to distinct microstructural evolutions. In simulation experiments R4 and R5, the pressure curves exhibit more pronounced fluctuations compared to R1, reflecting a higher probability and severity of particle breakage (Fig. 13(a)). Under the same applied stress, larger particles are more prone to reach their strength limit, owing to greater flaw populations and force magnitudes, and then shatter into multiple fragments. These new fragments must rearrange to accommodate further compression, triggering additional breakage cascades. By contrast, the smaller particles in R1 can better withstand the same stress (their individual loads are lower and they already pack more densely), so fewer particles fracture and fewer fragments form overall.

As compression proceeds, the influence of initial diameter becomes increasingly evident. At the maximum reduction of 19.5μm, R5 achieves a tortuosity of 1.8728 (slightly below R1's 1.8976), while its effective diffusivity rises to 0.1760, compared with 0.1590 in R1. Experiment R4 yields intermediate values (tortuosity = 1.8996, diffusivity = 0.1664). In other words, systems that begin with larger, and thus more extensively fractured, particles maintain marginally better pore connectivity and transport performance under heavy densification. Although all three cases converge to nearly the same final porosity (21.82–21.94 %), R5's tortuosity is about 1.3 % lower and its diffusivity about 11 % higher than R1's, with R4 showing a modest improvement over R1. These results underscore that, beyond simply preserving porosity, the initial size distribution controls how fracture reshapes the pore network and thus determines the ultimate balance between mechanical integrity and ionic transport.

4. Conclusions

This work presents a comprehensive framework for modelling, surrogate-assisted calibration, and design evaluation of particle breakage during LIB electrode calendering. By utilising the Tavares UFRJ particle replacement breakage model in the DEM framework, developing a dual-objective deep learning surrogate, and coupling these tools with inverse parameter inference and global sensitivity analysis, we have established a practical pathway from high-fidelity simulation to rapid design insights. The key conclusions are as follows:

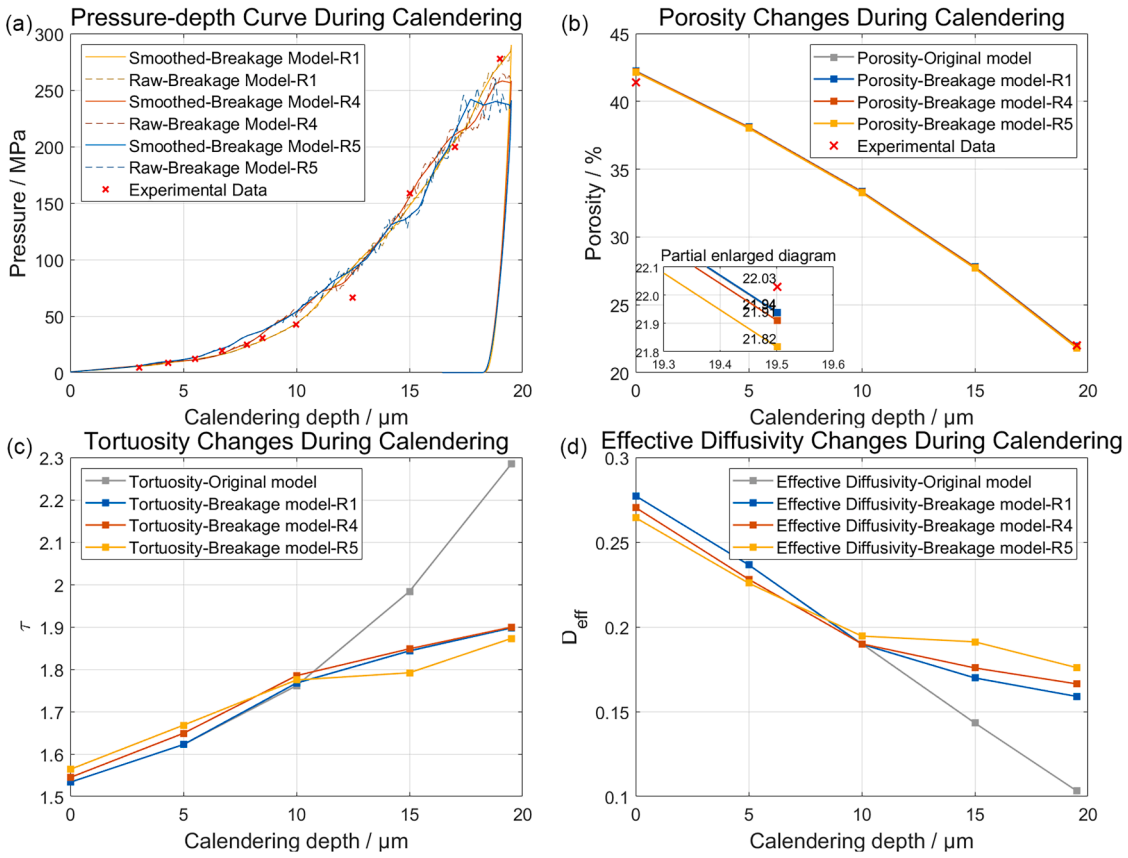

Fig. 13. Calendering-depth dependence of electrode mechanical and transport properties for three mean AM particle sizes: (a) pressure-depth curves, (b) porosity evolution, c) tortuosity evolution, and (d) effective diffusivity evolution. The experimental data are from Zhang et al. [28].

1. Integrated new breakage and surrogate approach reduces computational cost while preserving fidelity: Leveraging the sphere-based particle replacement model for electrode calendering simulation enables the characterisation of stress-induced fragmentation with significantly higher efficiency; specifically, it requires two orders of magnitude fewer particles than traditional full-bonded methods while maintaining predictive accuracy. The MLP surrogate simultaneously predicts compaction: pressure curves (MSE = 0.0003) and fracture statistic distributions (KL divergence = 0.33), demonstrating accurate macroscopic and microscopic behaviour at a fraction of the cost.
2. Efficient inverse calibration yields robust, reproducible predictions: A two-phase reverse-optimisation algorithm (Adam + L-BFGS) infers breakage parameters directly from pressure and fragment-size data. Forward DEM runs using the inferred parameters reproduce experimental pressure-depth trends with minimal run-to-run variability, confirming model reliability.
3. Global sensitivity analysis identifies dominant parameters for model simplification: Sobol indices highlight the characteristic size parameter (d_0) and fitting parameter (ϕ) as the primary drivers of compaction pressure and fracture distribution. In contrast, damage constant (γ) and truncation ratio exhibit negligible influence, suggesting they can be fixed in future applications to streamline calibration.
4. Particle breakage significantly improves electrode transport properties: Under severe calendering (19.5 μm reduction), inclusion of breakage produces ~20 % lower tortuosity and ~50 % higher effective diffusivity than non-fracture controls at equivalent porosity. Moreover, larger initial particles (10–12 μm vs.7.84 μm) further enhance pore connectivity, yielding marginally reduced tortuosity and increased diffusivity.

While the present framework demonstrates significant advances in efficient simulation and deep learning assisted calibration of particle breakage during electrode calendering, several limitations must be acknowledged. First, the sphere-based replacement model, although computationally expedient, cannot fully capture the anisotropic particle morphologies or non-spherical fracture patterns that occur in real electrodes. Second, the accuracy of the MLP surrogate model is currently validated only within the range of training data (specific compaction depths, material properties, and particle size distributions), which may limit its generalizability to new chemistries or processing conditions. Third, our simulations consider only quasi-static uniaxial compression and neglect dynamic effects, shear stresses, and thermal influences that are present in industrial calendering processes. Fourth, experimental validation has so far been limited to pressure-depth trends and fragment statistics; the impact on full-cell performance and long-term cycling remains to be assessed. Finally, the model presented in Reference [22] was originally developed to characterise fracture behaviour under unconstrained conditions, and consequently, it fails to account for the stabilisation effects induced by high coordination numbers. This omission may lead to a systematic bias in the parameters defining the fracture energy distribution. Specifically, the parameter representing the upper limit of fracture energy, E_∞, may be overestimated. This discrepancy arises because the model neglects the enhancement of a particle's load-bearing capacity when subjected to extreme confinement, where the surrounding particles provide structural support that inhibits crack propagation and premature failure. Future work will address these gaps by extending the training domain to include multi-axial loading scenarios and temperature-dependent behaviour, and performing targeted experiments to link microstructural evolution to electrochemical performance. Moreover, integrating this workflow within a multi-scale modelling platform will enable predictive design of electrodes under

realistic manufacturing and operating conditions.

Data availability

No data was used for the research described in the article.

CRediT authorship contribution statement

Jiashen Chen: Writing – review & editing, Writing – original draft, Visualization, Validation, Software, Methodology, Investigation, Conceptualization. **Maryam Asachi:** Writing – review & editing, Supervision. **Ali Hassanpour:** Writing – review & editing, Supervision. **Meisam Babaie:** Writing – review & editing, Supervision, Conceptualization. **Masoud Jabbari:** Writing – review & editing, Supervision, Conceptualization.

Declaration of competing interest

The authors declare that they have no known competing financial interests or personal relationships that could have appeared to influence the work reported in this paper.

Acknowledgements

For the purpose of open access, the author has applied a Creative Commons Attribution (CC BY) license to any Author Accepted Manuscript version arising from this submission.

References

[1] X. Lai, Q. Chen, X. Tang, Y. Zhou, F. Gao, Y. Guo, R. Bhagat, Y. Zheng, Critical review of life cycle assessment of lithium-ion batteries for electric vehicles: a lifespan perspective, eTransportation 12 (2022) 100169.
[2] E. Megan Mcgovern, D. Dmitriy Bruder, D. Erik Huemiller, J. Teresa Rinker, T. Jennifer Bracey, C. Ryan Sekol, A. Jeffrey Abell, A review of research needs in nondestructive evaluation for quality verification in electric vehicle lithium-ion battery cell manufacturing, J. Power. Sources. 561 (2023) 232742.
[3] M. Chouchane, N.E Primo, A. Alejandro Franco, Mesoscale effects in the extraction of the solid-state lithium diffusion coefficient values of battery active materials: physical insights from 3d modeling, J. Phys. Chem. Lett. 11 (7) (2020) 2775–2780.
[4] E. Mark Ferraro, L. Bradley Trembacki, E. Victor Brunini, R. David Noble, A. Scott Roberts, Electrode mesoscale as a collection of particles: coupled electrochemical and mechanical analysis of nmc cathodes, J. Electrochem. Soc. 167 (1) (2020) 013543.
[5] DL. Wood, M. Wood, J. Li, Z. Du, RE. Ruther, KA. Hays, N. Muralidharan, L. Geng, C. Mao, I. Belharouak, Perspectives on the relationship between materials chemistry and roll-to-roll electrode manufacturing for high-energy lithium-ion batteries, Energy Storage Mater. 29 (2020) 254–265.
[6] A. Shodiev, E. Primo, O. Arcelus, M. Chouchane, M. Osenberg, A. Hilger, I. Manke, J. Li, A.A. Franco, Insight on electrolyte infiltration of lithium ion battery electrodes by means of a new three-dimensional-resolved lattice boltzmann model, Energy Storage Mater. 38 (2021) 80–92.
[7] X. Lu, R.S Daemi, A. Bertei, D.R. Matthew Kok, B. Kieran O'Regan, L. Rasha, J. Park, G. Hinds, E. Kendrick, J.L. Dan Brett, R. Paul Shearing, Microstructural evolution of battery electrodes during calendering, Joule 4 (12) (2020) 2746–2768.
[8] S. Sandooghdar, J. Chen, M. Asachi, A. Hassanpour, E. Hosseinzadeh, M. Babaie, M. Jabbari, Pore-scale prediction of transport properties in lithium-ion battery cathodes during calendering using dem and cfd simulations, Powder. Technol. 453 (2025) 120601.
[9] K. Shi, A. Hassanpour, M. Babaie, M. Jabbari, Modelling of dry manufacturing of lfp cathode filaments with twin-screw extruder using the discrete element method, Particuology 109 (2026) 1–11.
[10] D. Schreiner, A. Klinger, G. Reinhart, Modeling of the calendering process for lithium-ion batteries with dem simulation, Procedia CIRP. 93 (2020) 149–155.
[11] R. Ge, D.J. Cumming, R.M. Smith, Discrete element method (dem) analysis of lithium ion battery electrode structures from x-ray tomography-the effect of calendering conditions, Powder. Technol. 403 (2022).
[12] R. Ge, A.M. Boyce, Y.S. Zhang, P.R. Shearing, D.J. Cumming, R.M. Smith, Discrete element method and electrochemical modelling of lithium ion cathode structures characterised by x-ray computed tomography, Chem. Eng. J. 465 (2023).
[13] M. Nikpour, B.A. Mazzeo, D.R. Wheeler, A model for investigating sources of li-ion battery electrode heterogeneity: part ii. active material size, shape, orientation, and stiffness, J. Electrochem. Soc. 168 (12) (2021) 120518.
[14] A. Lundkvist, P.-L. Larsson, E. Olsson, A discrete element analysis of the mechanical behaviour of a lithium-ion battery electrode active layer, Powder. Technol. 425 (2023).
[15] M. Lippke, C. Willuhn, T. Ohnimus, T. Heckmann, P. Scharfer, W. Schabel, C. Schilde, A. Kwade, Coupled numerical simulation of the drying and calendering for lithium-ion battery anodes with non-spherical particles, Powder. Technol. 452 (2025) 120566.
[16] R. Li, W. Li, A. Singh, D. Ren, Z. Hou, M. Ouyang, Effect of external pressure and internal stress on battery performance and lifespan, Energy Storage Mater. 52 (2022) 395–429.
[17] A. Asheri, S. Rezaei, V. Glavas, B.X. Xu, Microstructure impact on chemo-mechanical fracture of polycrystalline lithium-ion battery cathode materials, Eng. Fract. Mech. 309 (2024) 110370.
[18] F. Pistorio, D. Clerici, F. Mocera, A. Somà, Review on the numerical modeling of fracture in active materials for lithium ion batteries, J. Power. Sources. 566 (2023) 232875.
[19] J. Xu, AC. Ngandjong, C. Liu, FM. Zanotto, O. Arcelus, A. Demortière, A.A. Franco, Lithium ion battery electrode manufacturing model accounting for 3d realistic shapes of active material particles, J. Power. Sources. 554 (2023).
[20] J. Xu, B. Paredes-Goyes, Z. Su, M. Scheel, T. Weitkamp, A. Demortière, A.A. Franco, Computational model for predicting particle fracture during electrode calendering, Batter. Supercaps. 6 (12) (2023).
[21] L. Orefice, J.G. Khinast, Deformable and breakable dem particle clusters for modelling compression of plastic and brittle porous materials — model and structure properties, Powder. Technol. 368 (2020) 90–104.
[22] M.L. Tavares, A.V Rodriguez, M. Sousani, B.C. Padros, Y. Jin Ooi, An effective sphere-based model for breakage simulation in dem, Powder. Technol. 392 (2021) 473–488.
[23] M.T Campos, M. Powell, M.L. Tavares, Exploring the transition from single-particle to confined-particle-bed breakage by slow compression, Powder. Technol. 460 (2025) 120949.
[24] U. Vijay, E.D Galvez-Aranda, M. Franco Zanotto, T. Le-Dinh, M. Alabdali, M. Asch, A. Alejandro Franco, A hybrid modelling approach coupling physics-based simulation and deep learning for battery electrode manufacturing simulations, Energy Storage Mater. 75 (2025) 103883.
[25] E. Diego Galvez-Aranda, U.V. Le Tan Dinh, M. Franco Zanotto, A. Alejandro Franco, Time-dependent deep learning manufacturing process model for battery electrode microstructure prediction, Adv. Energy Mater. 14 (15) (2024).
[26] M. Duquesnoy, C. Liu, D.Z. Dominguez, V. Kumar, E. Ayerbe, AA. Franco, Machine learning-assisted multi-objective optimization of battery manufacturing from synthetic data generated by physics-based simulations, Energy Storage Mater. 56 (2023) 50–61.
[27] J. Chen, M. Asachi, A. Hassanpour, M. Babaie, M. Jabbari, Modelling of lithium-ion battery electrode calendering: a critical review, J. Energy Storage 123 (2025) 116702.
[28] J. Zhang, H. Huang, J. Sun, Investigation on mechanical and microstructural evolution of lithium-ion battery electrode during the calendering process, Powder. Technol. 409 (2022) 117828.
[29] J. Liu, W. Lin, Z. Wang, Y. Wang, T. Chen, J. Zheng, Elastic mechanics study of layered li(nixmnycoz)o2, PRX Energy 3 (1) (2024).
[30] J. Zhang, J. Sun, H. Huang, Z. Yuan, Influence of calendering process on the structural mechanics and heat transfer characteristics of lithium-ion battery electrodes via dem simulations, Particuology 85 (2024) 252–267.
[31] A.D. Renzo, F.P.D. Maio, An improved integral non-linear model for the contact of particles in distinct element simulations, Chem. Eng. Sci. 60 (5) (2005) 1303–1312.
[32] D.O. Potyondy, P.A. Cundall, A bonded-particle model for rock, Int. J. Rock. Mech. Min. Sci. 41 (8) (2004) 1329–1364.
[33] M.L. Tavares, D.S.A. Chagas, A stochastic particle replacement strategy for simulating breakage in dem, Powder. Technol. 377 (2021) 222–232.
[34] R. Liu, Y. Li, L. Tao, D. Liang, H.T. Zheng, Are we ready for a new paradigm shift? A survey on visual deep mlp, Patterns 3 (7) (2022) 100520.
[35] S.J. Cooper, A. Bertei, P.R. Shearing, J.A. Kilner, N.P. Brandon, Taufactor: an open-source application for calculating tortuosity factors from tomographic data, SoftwareX 5 (2016) 203–210.
[36] D. Li, C. Shen, Y. Zheng, J. Xu, Electrochemo-mechanical degradation and failure of active particles in high energy density batteries: a review, Small 21 (8) (2025).
[37] V. Nagda, H. Ekström, A. Kulachenko, Impact of mechanical degradation in polycrystalline nmc particle on the electrochemical performance of lithium-ion batteries, J. Electrochem. Soc. 171 (6) (2024) 060526.